Am J Cancer Res 2024;14(5):2584-2607
www.ajcr.us /ISSN:2156-6976/ajcr0156027

Original Article

Panoramic analysis of cell death patterns reveals prognostic and immune profiles of head and neck squamous cell carcinoma

Xinyu Liu[1*], Rui Miao[2,3*], Kui Liu[1], Qun Xie[1], Penghui Zheng[1], Junai Zhu[4], Ying Zhang[1], Fusen Peng[1]

[1]Department of Otolaryngology Head and Neck Surgery, Loudi Central Hospital, Loudi 417011, Hunan, The People's Republic of China; [2]Department of Otolaryngology Head and Neck Surgery, Xiangya Hospital, Central South University, No. 87 Xiangya Road, Changsha 410008, Hunan, The People's Republic of China; [3]Otolaryngology Major Disease Research Key Laboratory of Hunan Province, No. 87 Xiangya Road, Changsha 410008, Hunan, The People's Republic of China; [4]Department of Gastroenterology, The Chinese University of Hong Kong, Hong Kong SAR, China. [*]Equal contributors.

Received February 21, 2024; Accepted May 15, 2024; Epub May 15, 2024; Published May 30, 2024

Abstract: Head and neck squamous cell carcinoma (HNSCC) has been characterized by a low therapeutic response and poor prognosis. Currently, there are no reliable predictive models for HNSCC progression and therapeutic efficacy. This study explores the role of diverse patterns of cell death in tumor development, positing them as predictive factors of HNSCC prognosis. We utilized bulk transcriptome and single-cell transcriptome, align with clinical information from TCGA and GEO database, to analyze genes associated with 15 types of cell death and construct a cell death index (CDI) signature. The associations of CDI with tumor-infiltrating immune cells and immunotherapy-related biomarkers were also evaluated using various algorithms. The CDI signature emerged as a robust prognosis biomarker that could identify patients who can benefit potentially from immunotherapy, thus improving diagnostic accuracy and optimizing clinical decisions in HNSCC management. Notably, we discovered that CAAP1 deficiency not only induced apoptosis but also enhanced anti-tumor immunity, suggesting its potential as a target for clinical drug development.

Keywords: Cell death, intrinsic apoptosis, extrinsic apoptosis, head and neck squamous cell carcinoma, CAAP1, CD8+ T

Introduction

As one of the most common malignancies worldwide, head and neck squamous cell carcinoma (HNSCC) is characterized by a dismal 5-year overall survival (OS) rate of less than 35% [1, 2]. Heterogeneity is a hallmark of HNSCC, arising from various anatomic sites and associated with multiple of risk factors, including chronic human papillomavirus (HPV) infection, tobacco abuse, excessive alcohol consumption [3, 4]. HNSCC patients frequently experience recurrences in local and regional area, lymph nodes metastases, and exhibit high resistance to radiotherapy and chemotherapy alone or in combination [5, 6]. The poor therapeutic response is partly due to cells' ability to prevent cell death [7-9], although other factors such as increased proliferation, invasion, and metastasis also contribute to this phenomenon. Therefore, a deep understanding of cellular mechanisms and signaling pathways governing cell death in HNSCC is indispensable for improving risk stratification and predicting therapeutics benefits.

Cell death is a physiological process essential for maintaining tissue homeostasis or proper development, yet it can become pathogenic, undermining normal organ function and inducing inflammatory response [10]. Based on functional characteristics, cell death can be categorized into accidental cell death (ACD) and regulated cell death (RCD) [11]. ACD is an uncontrolled process triggered by unexpected danger signals, whereas RCD is precisely regulated by

https://doi.org/10.62347/PMDA6193

signaling cascades and effector molecules. Since 1972, research on RCD has predominantly focused on apoptosis [12], which is crucial for maintaining the balance and health of multicellular organisms [13]. In the context of HNSCC, the role of apoptosis is complicated [14]. On the one hand, it prevents HNSCC by removing mutated or stressed cells, especially in the early stages of cancer, where triggering apoptosis can halt the progression and spread of cancer cells [15]. On the other hand, HNSCC cells often develop mechanisms to avoid apoptosis, aiding their survive and proliferation despite genetic damage [16]. Most HNSCC treatments still rely heavily on apoptosis.

Two major subtypes of apoptosis have been established, extrinsic and intrinsic apoptosis, respectively. Extrinsic apoptosis is triggered by stimuli from extracellular microenvironments detected by membrane receptors especially death receptors and TNF receptor, driven by caspases CASP8 or CASP10 [11, 17, 18]. In contrast, the intrinsic pathway starts inside the cell, often due to DNA damage or stress. Here, the mitochondria release a molecule called cytochrome c, which teams up with Apaf-1 and caspase-9 to form a complex that activates caspase-3 and caspase-7 leading to cell death [19]. Extrinsic apoptosis and intrinsic apoptosis share the same effector caspases: CASP3, CASP6, and CASP7 [11]. The biological characteristic and therapeutic response of HNSCC can be further shaped by apoptosis [7, 20-22]. Over the past few years, it has been identified that there are many novel forms of non-apoptotic RCD including necroptosis, ferroptosis, pyroptosis, netotic cell death, entotic cell death, lysosome-dependent cell death, parthanatos, autophagy-dependent cell death, oxeiptosis and alkaliptosis [11, 12]. Some of non-apoptotic RCD such as necroptosis, ferroptosis, pyroptosis and autophagy can be observed in the setting of cell development and viral infection, implying specific physiological significance and exposing effects on HNSCC tumorgenesis [9, 23-25]. Nevertheless, others (like netotic cell death, entotic cell death, lysosome-dependent cell death, parthanatos etc.) might also be involved in HNSCC biology but be rarely studied, which needs further exploration.

In our study, for training and validation cohorts, we collected 492 patients from the TCGA, 109 patients from GSE27020, 348 patients from IMvigor210. For single-cell RNA transcriptome datasets, we collected 6 patients from GSE164690. We incorporated apoptotic RCD and non-apoptotic RCD related genes and selected the genes which were tightly related to HNSCC survival and prognosis. Then we established the CDI signature based on above genes and further explored the difference of prognosis, immune infiltration and signaling pathway in high and low CDI group, offering insights into prognosis prediction and immune landscape in HNSCC. The flowchart of this study was shown in **Figure 1**.

Methods

Data collection

The key regulatory genes were identified for 15 cell death patterns and a combination of GSEA gene sets, KEGG, review articles, and manual collation of gene sets was used to collect genes [11, 12]. Altogether, 33 pyroptosis genes, 283 ferroptosis genes, 231 autophagy genes, 23 entotic cell death genes, 15 cuproptosis genes, 9 parthanatos genes, 27 anoikis genes, 194 lysosome-dependent cell death genes, 630 necroptosis genes, 5839 intrinsic apoptosis genes, 2129 extrinsic apoptosis genes, 9218 necrosis genes, 1736 immunologic cell death genes, 146 apoptosis-like morphology genes and 73 necrosis-like morphology genes were collected (Table S1).

Raw bulk transcriptome counts, normalized and log2 converted RNA-sequencing profiles FPKM as well as clinical information for 492 HNSCC patients and 44 normal samples were collected from the University of California Santa Cruz (UCSC) database. To convert ensemble ids into gene symbols, the "GeoTcgaData" R package was applied. From the Gene Expression Omnibus (GEO) database (IDs: GSE27020 and GSE41613), log2 converted chip-seq data and clinical characteristics of 109 and 97 HNSCC patients were obtained, respectively. GSE164690 were used to collect single-cell RNA transcriptome data for HNSCC patients, and the Serat V4 R package was used for analysis.

Identification of cell death related genes associated with HNSCC prognosis

First, univariate Cox regression was used to screen prognosis-associated genes in 15 cell

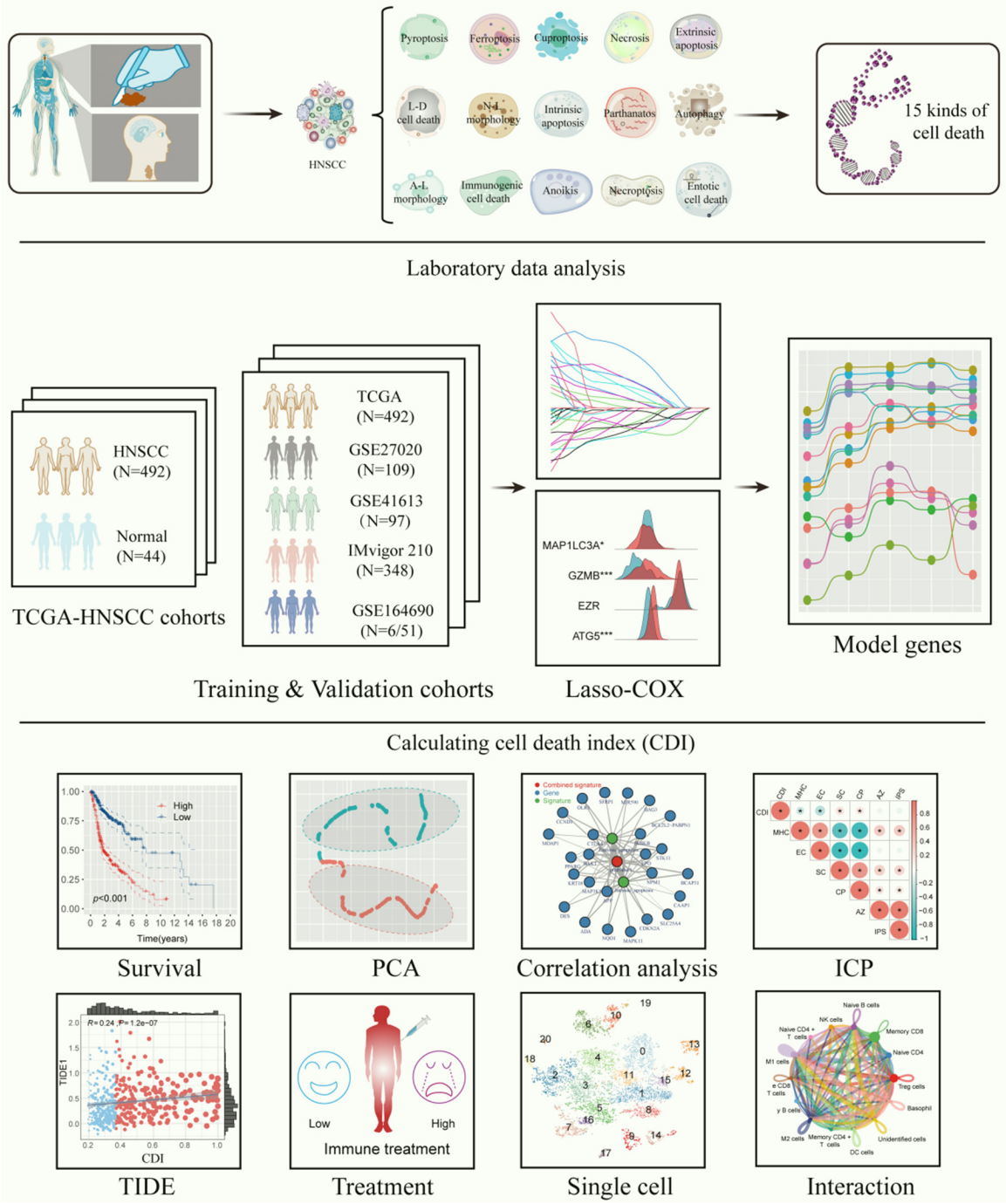

Figure 1. Flowchart for comprehensive analysis of different cell death modes in patients with head and neck squamous cell carcinoma (HNSCC).

death types. After LASSO analysis incorporated into multivariate Cox regression model, the cell death-related genes closely associated with HNSCC prognosis were further screened. In addition, the expression differences of the screened genes in tumor and normal tissues were further compared.

The establishment and validation of cell death related prognosis signature

We calculated the CDI of each patient using prognostic cell death related genes expression based on the following model formula: CDI = ΣiCoefficient (mRNAi) × Expression (mRNAi).

The cut-off value was determined by the "surv_cutpoint" function of the R package "survminer", which calculates statistics based on maximally selected rank statistics. The principle of this function to determine the optimal cutoff value is to obtain the two groups with the most statistically significant difference in survival rates through multiple simulations. The predictive reliability of the cell death related signature was assessed through time-related receiver operating characteristic (ROC). The two cell death-related features with the highest AUC values were screened and combined signatures were constructed by generalized linear model (GLM). The Kaplan-Meier survival curve was performed to compare the overall survival (OS) between the high and low CDI groups. Meanwhile, the results were also validated in the GSE27020 and GSE41613 cohort.

Immune infiltration analysis

The relationship between CDI signature and immune infiltration was identified using the TIMER2.0 database (http://timer.comp-genomics.org). Immunedeconv, an R package integrating six state-of-the-art algorithms including: TIMER, xCell, MCP-counter, CIBERSORT, EPIC, and quanTIseq was utilized [26]. These algorithms were systematically benchmarked, and each was found to have unique properties and strengths. The "microenvironment cell population count (MCP-counter)" method was applied to assess the immune infiltration. The MCP-counter generates absolute abundance scores for ten immune cell and stromal cell populations based on the normalized FPKM expression matrix converted by log2 [27]. Besides, the enrichment of 22 immune cells was inferred by the CIBERSORT algorithm [28]. CIBERSORT can compute the abundance of specific cell types in a mixed sample based on the bulk expression. The ESTIMATE algorithm was used to analysis the difference of stromal score, immune score and ESTIMATE score by the R package "estimate" [29]. To better predict the immunotherapy response, we used ggplot2 package and violin plot visualization to study the relationship between the model and the ICIs-related biomarkers. The algorithm called Tumor Immune Dysfunction and Exclusion (TIDE) was used to model two primary mechanisms of tumor immune evasion. Based on TIDE algorithm, the immunotherapy response between two groups was predicted.

Gene set enrichment analyses

To better access the biological functions and pathways of the CDI signature, we performed Gene Set Enrichment Analyses (GSEA) through R packages "clustersProfiler", "enrichplot" and "ggplot2". The gene sets "c2.cp.kegg.v7.4.symbols.gmt" and "h.all.v7.4.symbols.gmt" were chosen as the reference gene set. The normalized enrichment score (|NES|>1), nominal *P* value <0.05 (NOM *P* value), and FDR adjusted q-value <0.25 were considered as significant pathway enrichment.

Visualization

ScRNA-seq data were quality controlled prior to analysis, and cells with >25% of mitochondria-associated genes were filtered out. The top 2000 highly variable genes of each sample were normalized using the ScaleData function based on variance stabilization transformation (vst). The dimensionality of the PCA was reduced using the RunPCA function. We chose dim = 20 and clustered the cells into different cell groups using "FindNeighbors" and "FindClusters" functions. The resolution was 0.5. T-SNE (t-distributed stochastic neighbor embedding), a nonlinear dimension reduction method in seurat was applied, to map high dimensional cellular data into a two-dimensional space, grouping cells with similar expression patterns and separating those with different expression patterns. As a result, the differences between cells became more apparent. In the following step, we made annotations for each cell type using SingleR. The reference cells was used by SingleR to identify cell types in order to identify the similar expression pattern between the cells.

Pseudotime analysis

An analysis of pseudotime, also known as cell trajectory analysis, helps predict the evolutionary trajectory of apoptosis pathways and cell subtypes and infer the differentiation trajectory of stem cells during disease progression. By analyzing key gene expression patterns using Monocle 2, we performed pseudotime analysis in the current study. The pseudotime value was used by monocle to model the gene expression level as a nonlinear smooth pseudotime function to show change in gene expression with

time. FDR<1e-5 was regarded as significant difference.

Cell-cell interaction analysis

Based on the ligand-receptor information, we used the single-cell gene expression matrix to unravel the communication between immune cell subtypes which was contained in CellChat software with default parameters, modelling the communication probability and identifying significant communications.

Cell culture

Fadu and HN8 cells were obtained from the American Type Culture Collection (ATCC), both cells were grown in Dulbecco's modified Eagle's medium (DMEM) supplemented with 10% (v/v) fetal bovine serum (FBS, Inner Mongolia Opcel Biotechnology Co., Ltd). Meer was obtained from Dr. Zhuo Chen (the Cancer Research Center at Emory University, USA) and grown in Meer-MEM supplemented with 10% (v/v) FBS at 37°C in a 5% CO_2 incubator. Polyethylenimine (sigma, 408727) was used for transient transfection of plasmid DNA into 293T cells.

CRISPR-Cas9 knockout cells

Two guide RNAs (gRNAs), with sequences 5'-CAGCAGTGCTTCTGTATTAT-3' and 5'-ATAATACAGAAGCACTGCTG-3' were strategically employed to target CAAP1 (human), whereas 5'-CCTTTACTTACCCTTTGGGA-3' and 5'-TCCCAAAGGGTAAGTAAAGG-3' were utilized to target BCL2L2-PABPN1 (human), Sg1, 5'-CAACGCGGGTACGATGTCCG-3', Sg2, 5'-TGACGGGGAAAAAGTCCTCC-3' were strategically employed to target CAAP1 (mouse). Subsequently, these meticulously chosen gRNAs were incorporated into the gRNA-expression plasmid, lentiGuide-Puro. The gRNA-expressing cellular entities underwent a rigorous selection process employing 2 μg/ml puromycin before being subjected to flow cytometry sorting. The resultant singular clones were cultured with precision in 96-well plates for an additional 10-14 days or an extended duration, contingent upon the cellular growth rate.

Western blot and reagents

Proteins were meticulously separated utilizing 10% SDS-PAGE, and subsequently, they were transferred onto nitrocellulose membranes (Bio-Rad). For the purpose of immunoblotting, the following antibodies were employed at a dilution of 1:1000: rabbit anti-CAAP1 antibody (PA5-54977, Thermofisher), rabbit anti-BCL2L2-PABPN1 antibody (NBP2-61706, NOVUS), rabbit anti-caspase 8 antibody (9746S, CST), rabbit anti-caspase 9 antibody (10380-AP, proteintech) and rabbit anti-Vinculin antibody (ab129002, Abcam); and mouse anti-GAPDH (60004-1-Ig, Proteintech).

The experiments involved the utilization of recombinant human TNF-α (rcyc-htnfa) sourced from Invivogen. Cycloheximide (CHX, S7418) were procured from Selleck and ABT-737 (HY-50907) were procured from MCE.

Migration assays

The cells were artfully situated on Transwell migration chambers, furnished with 8 μm pore polycarbonate membrane inserts (Corning, Sigma-Aldrich, Deisenhofen, Germany). Within these chambers, a medium with 5% FCS graced the upper compartment, while the lower chamber boasted 20% FCS, facilitating an elegant transmigration period spanning 48 hours. Following this period, any non-transmigrated cells were tenderly eliminated with the assistance of a cotton-tipped applicator, and the filters were subsequently adorned with a cell staining solution. The enumeration of transmigrated cells unfolded with meticulous precision under the captivating lens of a 100-fold magnification.

For the beguiling scratch wounding experiments, the confluent monolayers of cells were "wounded" by gentle scratching with 200 μl universal pipet tips. The width of the wound cleft was assessed after a mesmerizing 24 hours, within three optical fields. The measurements from each field were averaged, and any discernible differences were tested for their significance.

Determination of levels of Bax via ELISA

Serum was collected from each group of cells, centrifuged at 2,500× g at 4°C for 10 min, and the supernatant was aspirated. Each well was added with the standard to plot the standard curves, and then with 30 μl of buffer, 20 μl each of standard and sample, separately,

and 50 μl of antibody solution. The fluid was removed, and the resulting sample and standard were cleaned by washing 3 times, adding 100 μl of enzyme solution, and then reacted for 30 min, washed again, and reacted with 100 μl of substrate solution for 15 min. The reaction was terminated by adding 100 μl of stop solution. Finally, the absorbance was measured using a microplate reader to calculate the content of Bax.

Caspase-8 activity

Caspase-8 activity was assessed using a caspase-8 enzymatic assay kit sourced from Abcam (Cambridge, MA). In brief, post-treatments, cells were resuspended in chilled cell lysis buffer and incubated on ice for 10 minutes. Subsequently, cell lysates were subjected to centrifugation for 1 minute at 10,000× g. Supernatants were harvested, assayed for protein concentration, and kept on ice until analysis. For each sample, 100 μg of protein was utilized and diluted in 50 μl of cell lysis buffer. To each sample, 50 μl of the provided 2× reaction buffer and 5 μl of the 4 mM acetyl-Ile-Glu-Thr-Asp p-nitroaniline (IETD-pNA) substrate were added. The samples underwent incubation at 37°C for 1 hour, were subsequently transferred to a microtiter plate, and their absorbance was read at 405 nm in a microplate reader.

Flow cytometry

Fadu and HN8 underwent treatment with diverse chemotherapeutic agents, as specified. Subsequently, cells were harvested, cleansed with PBS on two occasions, and subjected to staining utilizing the Annexin V-FITC/PI Apoptosis Assay Kit (Beyotime Biotechnology), adhering meticulously to the directives furnished by the manufacturer. The stained cellular specimens underwent scrutiny employing a BD FACSAria III flow cytometer, and the acquired data were meticulously processed utilizing the FlowJo software. Annexin-V, with acumen, discerns phosphatidylserine exposed on the extrinsic leaflet of the plasma membrane in apoptotic cells.

Employing flow cytometry, we conducted an analysis of the composition of CD8+ T cells derived from peripheral blood and tumor tissue. Tumors were dissected, minced and digested with 1 mg/ml Collagenase/Dispase (Sigma-Aldrich, 10269638001) and 1× DNase I (Qiagen, 79254) at 37°C for 30 minutes. Bloods incubated with red blood cells lysis buffer. Dissociated tumor and peripheral blood mononuclear cells (PBMCs) were filtered through a 70 μm filter to achieve a single-cell suspension before staining for flow cytometry analysis. Cells were stained using Anti-CD8a PE (eBioscience, Cat#12-0081-82, 1:100), anti-CD3e PE-Cyanine7 (eBioscience, Cat#25-0037-42, 1:100), anti-CD3 PerCP-Cyanine5.5 (eBioscience, Cat#45-0037-42, 1:100), anti-Granzyme B FITC (eBioscience, Cat#11-8898-82, 1:100), and cells were fixed and permeabilized with True-Nuclear™ Transcription Factor Buffer Set (Biolegend, Cat#424401), and dead cells were stained with Ghost Dye™ Violet 510 (Cytek Biosciences, Cat#SKU 13-0870-T100) before fixation and permeabilization and excluded during analysis. Cells were imaged on a BD Biosciences LSRFortessa and analysed with Flowjo.

Mouse tumor model and treatment

The research protocol involving animal studies was approved by the Institutional Review Committee of Xiangya Hospital, Central South University. Male Nude mice and C57BL/6 mice aged 4-6 weeks were obtained from Hunan Slake Jingda Experimental Animal Co., Ltd. and housed at the Department of Animal Science, Central South University. CAAP1 knockout or control Fadu (2×10^6) or Meer (1×10^6) cells were subcutaneously injected into the dorsal flank of each nude or C57BL/6 mouse. At the end of four weeks, the mice were euthanized, and the tumors were harvested and weighed. Tumor sizes were measured every other day. Tumor volume was assessed employing the formula: the product of length and the square of width divided by two, with length denoting the utmost diameter of the tumor and width indicating the minimal diameter.

Statistical analysis

R version 4.1.3 was used for all statistical studies. The survival curve was plotted by Kaplan-Meier survival curve. Wilcoxon test was used to compare the differences between two groups, and Spearman analysis was used to calculate the correlation coefficients. Double-

tailed P<0.050 was considered statistically significant.

Results

The relationship of cell death related genes with HNSCC prognosis

We analyzed the differential expression of cell death related genes between normal and tumoral tissues in Figure S1. Intrinsic apoptosis related genes such as STK11, SLC25A4, PPARG, NPM1, MAPK11 etc. as well as extrinsic apoptosis related genes such as STK11, SFRP1, PPARG, OLR1, NPM1 etc. were significantly expressed in HNSCC tissues. Multivariate analysis showed that intrinsic apoptosis related genes including STK11 (HR = 0.726, 95% CI = 0.549-0.959), NPM1 (HR = 1.340, 95% CI = 1.015-1.770), MAPK11 (HR = 0.781, 95% CI = 0.646-0.943), IKBKB (HR = 0.735, 95% CI = 0.579-0.932), EPO (HR = 0.815, 95% CI = 0.678-0.979), DES (HR = 1.045, 95% CI = 1.003-1.088), CTLA4 (HR = 0.780, 95% CI = 0.677-0.898), CDKN2A (HR = 0.923, 95% CI = 0.871-0.978), CAAP1 (HR = 1.369, 95% CI = 1.081-1.734), BAK1 (HR = 1.276, 95% CI = 1.002-1.626) and APP (HR = 1.230, 95% CI = 1.007-1.503) as well as extrinsic apoptosis related genes including STK11 (HR = 0.642, 95% CI = 0.482-0.855), SFRP1 (HR = 0.912, 95% CI = 0.482-0.855), PPARG (HR = 1.266, 95% CI = 1.079-1.485), NPM1 (HR = 1.409, 95% CI = 1.083-1.833), MIR590 (HR = 0.840, 95% CI = 0.721-0.979), MAP3K5 (HR = 0.813, 95% CI = 0.667-0.992), CTLA4 (HR = 0.784, 95% CI = 0.676-0.910), BCL2L2-PABPN1 (HR = 1.465, 95% CI = 1.095-1.960), BAK1 (HR = 1.308, 95% CI = 1.040-1.644), APP (HR = 1.250, 95% CI = 1.022-1.530) were independent predictors of OS.

The establishment and validation of cell death index (CDI) signature

We established 15 types of cell death related signature according to the prognostic cell death related genes derived by univariate and multivariate analysis. The 1-, 2-, 3-, 4- and 5-year AUC value was calculated and compared among 15 types of cell death signature as shown in **Figure 2A**, **2B**. Intrinsic and extrinsic signature, which was named cell death index (CDI) signature by us had the superior predictive performance that the 1-, 2-, 3-, 4- and 5-year AUC value was 0.732, 0.773, 0.773, 0.777 and 0.770, respectively (**Figure 2B** and **2D**). The ROC curve also supported above conclusion that the 5-year AUC value of CDI signature was higher than that of intrinsic or extrinsic apoptotic signature in **Figure 2C**. Then, we divided HNSCC patients into high and low risk group based on CDI, intrinsic and extrinsic apoptosis levels, respectively. Log-rank test was conducted to further demonstrate the HNSCC survival difference between high and low risk group. The Kaplan-Meier survival curve has presented that the overall survival of HNSCC patients in low risk group was significantly longer than that of high risk group (P<0.05) (**Figure 2E-G**). Principle clustering analysis (PCA) also showed gene classification in high and low risk group in **Figure 2H-J**. Diagram of gene interaction network displayed that CDI signature was tightly associated with intrinsic and extrinsic apoptotic related genes, especially KRT18, PPARG, CTLA4, IKBKB, STK11, NPM1, APP, MAP3K5, BAK1, EPO (**Figure 2K**). As shown in **Figure 2L**, we could found that HNSCC patients in high CDI group tend to be in dead status while those in low CDI group tent to be in alive status. With the increase in CDI, survival rate in HNSCC patients decreased gradually.

To validate the predictivity of CDI signature, GSE27020 and GSE41613 cohort was applied. We firstly compared 1-, 2-, 3-, 4- and 5-year AUC value of CDI signature with intrinsic apoptotic and extrinsic apoptotic signature using GSE27020 and GSE41613 cohort (**Figure 3A** and **3H**). Subsequently, the correlation between OS and CDI, intrinsic apoptotic and extrinsic apoptotic signature was shown in Kaplan-Meier survival curve, respectively (**Figure 3B-D**, **3I-K**). PCA in GSE27020 and GSE41613 cohort showed gene classification in high and low CDI group (**Figure 3E-G**, **3L-N**). Based on above findings, we drew conclusion that the predictive capacity of CDI signature in HNSCC prognosis was verified successfully.

The association between immune cell infiltration and CDI signature

To illustrate the mechanism that CDI was strongly associated with HNSCC prognosis, we explored the immune cell infiltration in high and low CDI group. MCP counter was applied to

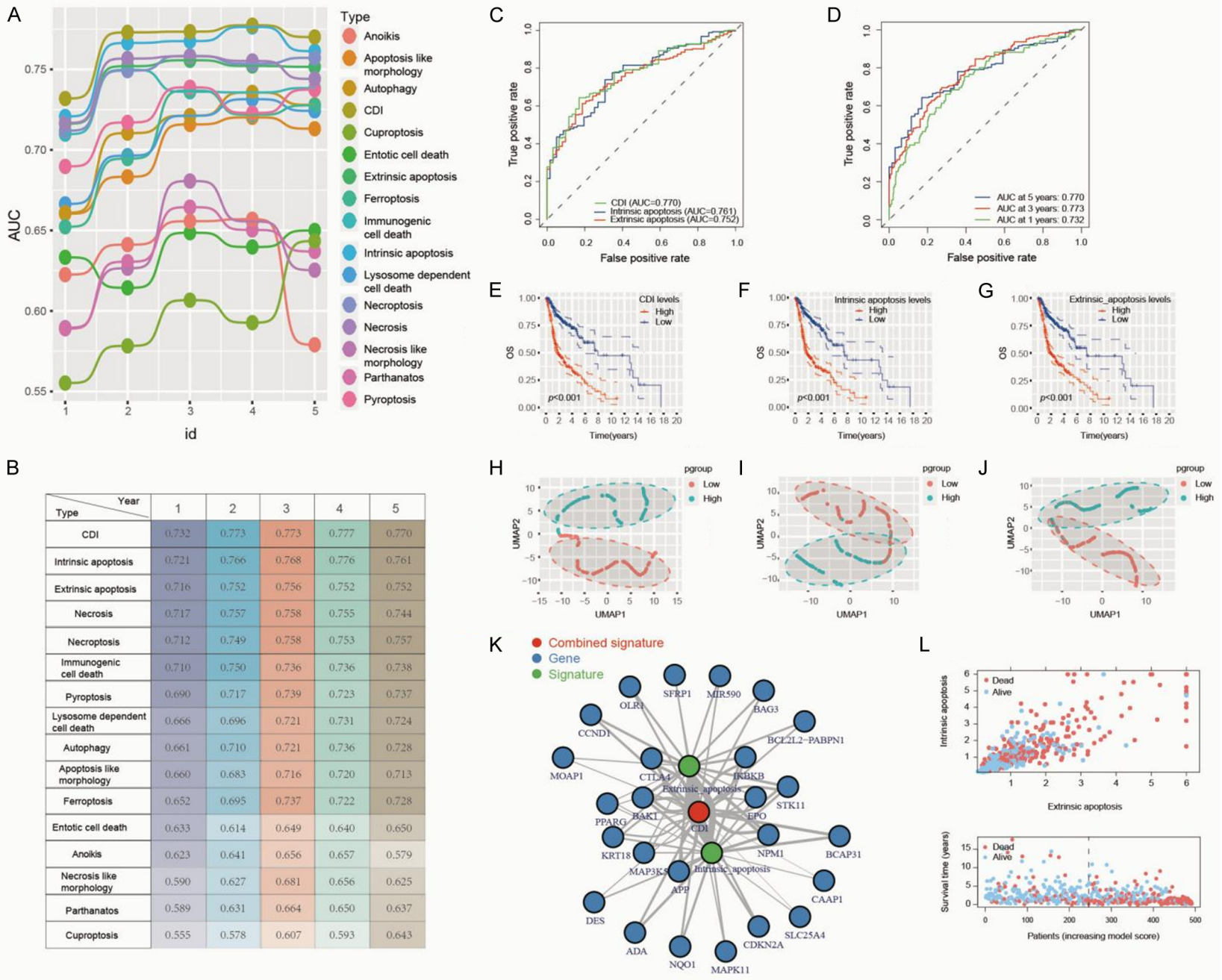

B

Type \ Year	1	2	3	4	5
CDI	0.732	0.773	0.773	0.777	0.770
Intrinsic apoptosis	0.721	0.766	0.768	0.776	0.761
Extrinsic apoptosis	0.716	0.752	0.756	0.752	0.752
Necrosis	0.717	0.757	0.758	0.755	0.744
Necroptosis	0.712	0.749	0.758	0.753	0.757
Immunogenic cell death	0.710	0.750	0.736	0.736	0.738
Pyroptosis	0.690	0.717	0.739	0.723	0.737
Lysosome dependent cell death	0.666	0.696	0.721	0.731	0.724
Autophagy	0.661	0.710	0.721	0.736	0.728
Apoptosis like morphology	0.660	0.683	0.716	0.720	0.713
Ferroptosis	0.652	0.695	0.737	0.722	0.728
Entotic cell death	0.633	0.614	0.649	0.640	0.650
Anoikis	0.623	0.641	0.656	0.657	0.579
Necrosis like morphology	0.590	0.627	0.681	0.656	0.625
Parthanatos	0.589	0.631	0.664	0.650	0.637
Cuproptosis	0.555	0.578	0.607	0.593	0.643

Figure 2. The prognosis value of CDI signature in HNSCC. A, B. A comparison of 1-, 2-, 3-, 4- and 5-year AUC value among 15 types of cell death signature showed the superiority of CDI signature. C. A comparison of ROC curve in CDI signature with intrinsic apoptotic signature and extrinsic apoptotic signature. D. The 1-, 3-, and 5-year ROC curve of CDI signature suggested that all AUC values were over 0.70. E-G. The Kaplan-Meier survival curve with log-rank test demonstrated the relationship between OS and CDI signature, intrinsic apoptotic signature and extrinsic apoptotic signature, respectively. H-J. Clustering analysis showed gene classification in high and low risk group based on CDI signature, intrinsic apoptotic signature and extrinsic apoptotic signature, respectively. K. Diagram of gene interaction network showed that CDI signature was tightly associated with intrinsic and extrinsic apoptotic related genes. L. The distribution of risk score based on intrinsic apoptotic signature and extrinsic apoptotic signature and survival status in high and low risk group based on CDI signature.

compare the infiltration level of 8 immune cells and 2 stromal cells populations in high and low CDI group (Figure S2A). The absolute abundance scores of T cells, CD8+ T cells, cytotoxic lymphocytes, B lineage, NK cells, myeloid dendritic cells was statistically higher in low CDI group while that of fibroblasts was higher in high CDI group. The relationship of CDI signature with 8 immune cells and 2 stromal cells populations using MCP counter was also presented in Figure S2B. In addition, we investigated the difference of 22 immune cells infiltration level between high and low CDI group using CIBERSORT algorithm (Figure S2C). The results showed that CD8+ T cells, B cells naïve, CD4+ memory activated T cells, follicular helper T cells and Tregs were mainly enriched in low CDI group. In contrast, M2 macrophages and CD4 memory resting T cells were significantly enriched in high CDI group (Figure S2C). The role of CDI signature in 22 immune cells infiltration using CIBERSORT algorithm was further unveiled (Figure S2D). The infiltration level of CD8+ T cells, B cells naïve, CD4+ memory activated T cells, follicular helper T cells and Tregs was negatively associated with CDI while that of M2 macrophages and CD4 memory resting T cells was positively associated with CDI (Figure S2D).

To avoid inaccuracy and bias of single algorithm, we also offered insights into the immune landscape in high and low CDI group using several algorithm including CIBERSORT, EPIC, QUANTISEQ, TIMER and XCELL. Figure S3A described the correlation of CDI with infiltration level of immune cells using CIBERSORT, EPIC, QUANTISEQ, TIMER and XCELL. The difference of immune cells infiltration level between high and low CDI group using above algorithm was presented in Figure S3B. We can conclude that infiltration level of B cells was negatively related with CDI when applying any of above algorithm. Similarly, B cells were more likely to enrich in high CDI group compared with low CDI group using any of above algorithm. Next, ESTIMATE algorithm was applied to compare ESITIMATE Score, IMMUNE Score, Stromal Score and Tumor Purity in high and low CDI group in Figure S3C-F. ESITIMATE Score, IMMUNE Score was higher in low CDI group while Tumor Purity was higher in high CDI group. The relationship of CDI with ESITIMATE Score, IMMUNE Score, Stromal Score and Tumor Purity was further elaborated in Figure S3G-J. Adverse correlation between ESITIMATE Score, IMMUNE Score and CDI was identified ($P<0.05$). Oppositely, positive correlation between Tumor Purity and CDI was identified ($P<0.05$).

Assessment of response to immunotherapy between high and low CDI group

Nowadays, cancer immunotherapy represented by ICIs offers a promising treatment option for recurrent and metastatic HNSCC [30]. To further elaborate the predictive role of CDI signature in immunotherapy, we examined the correlation between CDI and biomarkers that are associated with ICIs. The results indicated that the expression levels of CD274, CTLA4, IDO1, PDCD1, TIGIT, TNF, LAG3, HAVCR2 were upregulated in the low CDI group ($P<0.05$), implying that the low CDI group tended to benefit more from immunotherapy (**Figure 4A-H**). TIDE score is closely related with immune therapy resistance and immune escape in tumors microenvironment. A higher TIDE score indicates a higher likelihood of immune escape and a lower response rate of immunotherapy. As shown in **Figure 4I** and **4J**, compared with high CDI group, TIDE score in low CDI group was significantly lower and the CDI was positively related with TIDE score ($R = 0.24$, $P<0.05$), demonstrating low CDI group had higher response rates of immunotherapy. What's more, we computed the percentage of immunotherapy responders and non-responders in

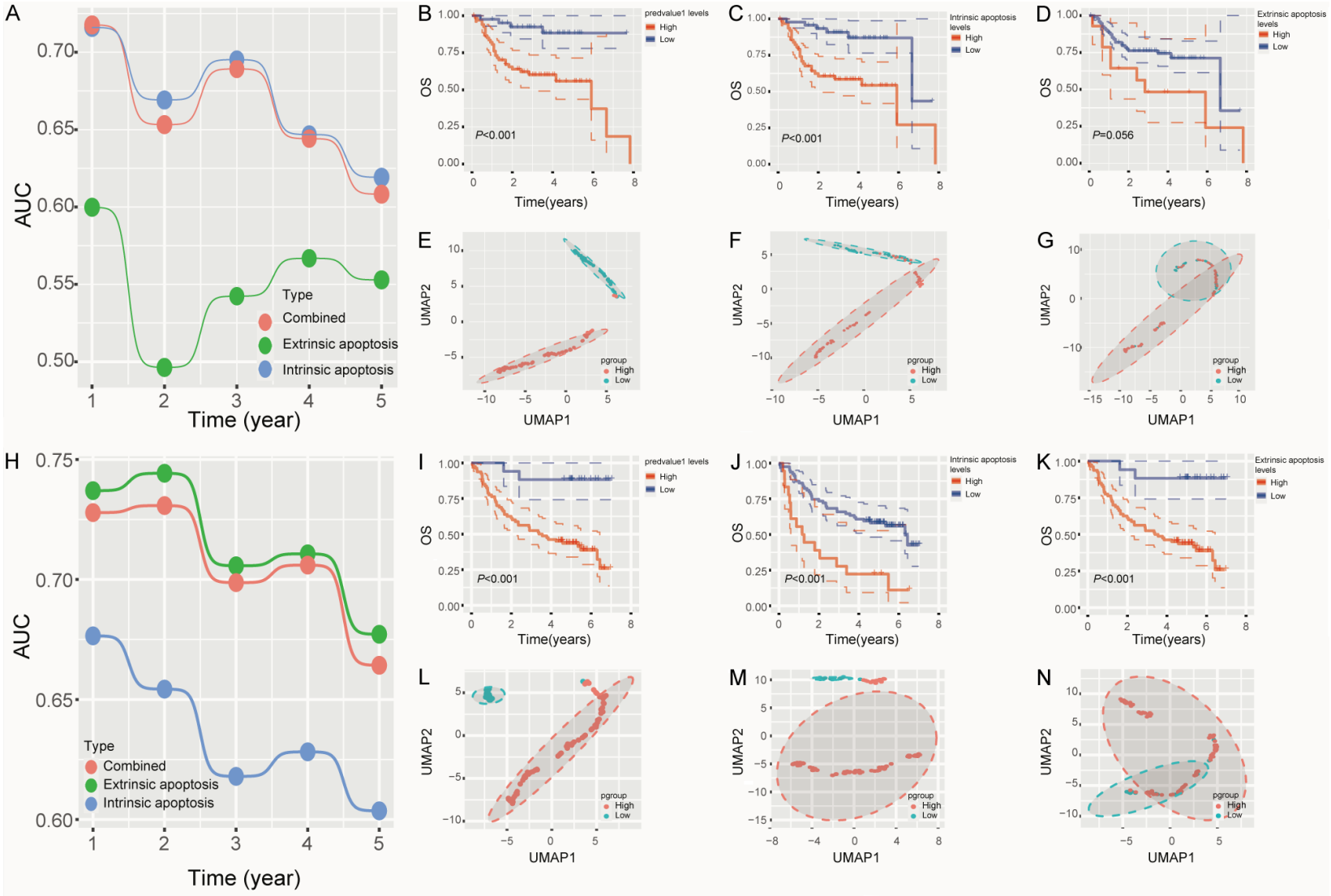

Figure 3. The validation of CDI signature in prognosis of HNSCC. A. A comparison of 1-, 2-, 3-, 4- and 5-year AUC value of CDI signature with intrinsic apoptotic signature and extrinsic apoptotic signature using GSE27020 cohort. B-D. The Kaplan-Meier survival curve with log-rank test using TCGA cohort demonstrated the relationship between OS and CDI signature, intrinsic apoptotic signature and extrinsic apoptotic signature, respectively. E-G. Clustering analysis using TCGA cohort showed gene classification in high and low risk group based on CDI signature, intrinsic apoptotic signature and extrinsic apoptotic signature, respectively. H. A comparison of 1-, 2-, 3-, 4- and 5-year AUC value of CDI signature with intrinsic apoptotic signature and extrinsic apoptotic signature using GSE65858 cohort. I-K.

The Kaplan-Meier survival curve with log-rank test using GSE cohort demonstrated the relationship between OS and CDI signature, intrinsic apoptotic signature and extrinsic apoptotic signature, respectively. L-N. Clustering analysis using GSE cohort showed gene classification in high and low risk group based on CDI signature, intrinsic apoptotic signature and extrinsic apoptotic signature, respectively.

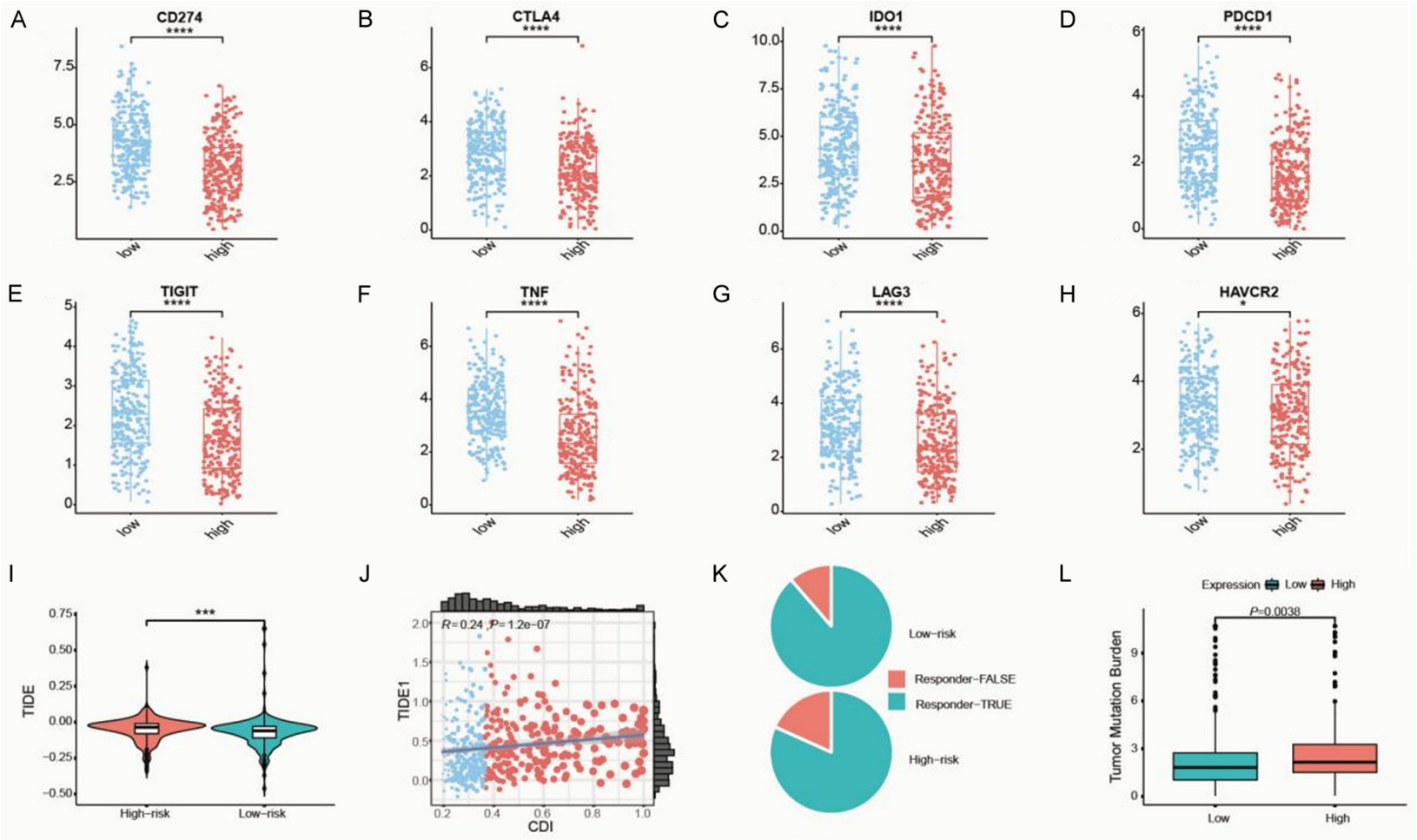

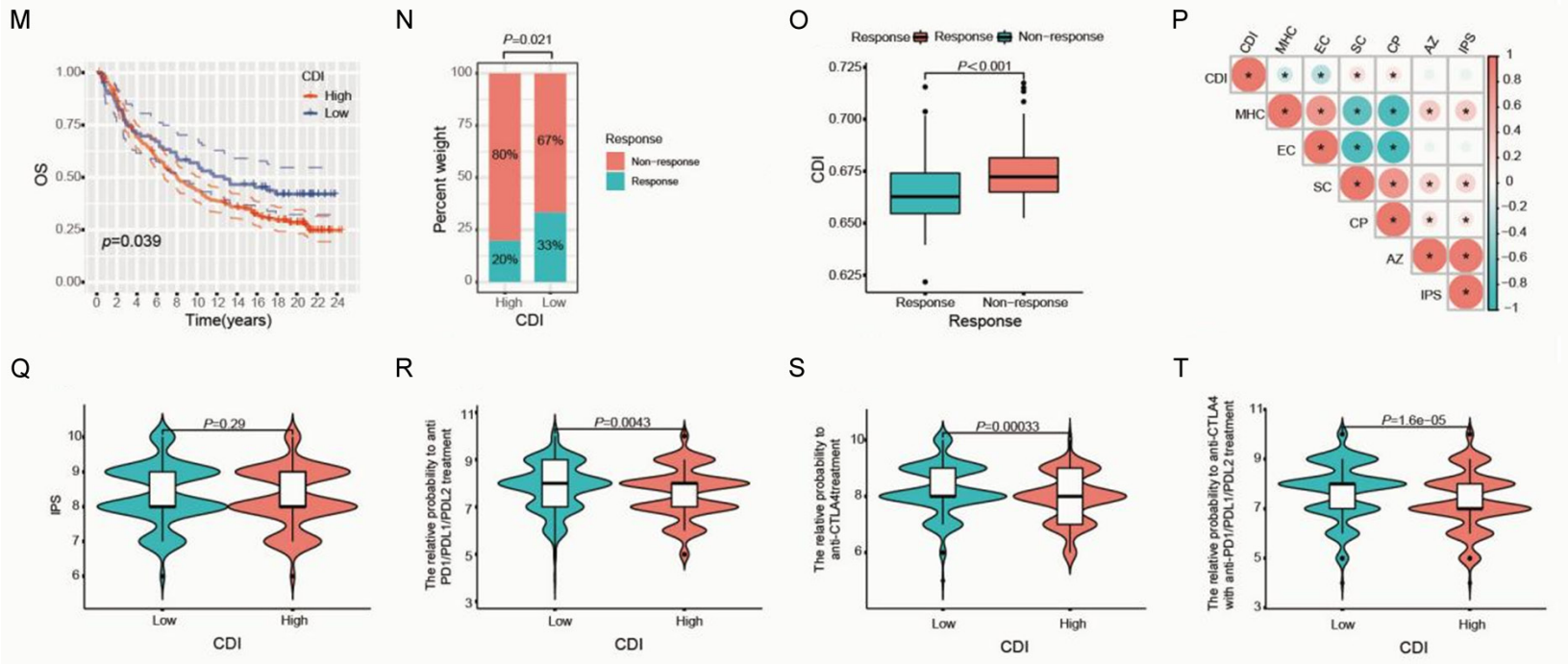

Figure 4. Correlation of CDI with immunotherapy related biomarkers. A-H. The difference of immune checkpoints between high and low CDI group. I. The difference of TIDE score between high and low CDI group. J. The relationship of CDI with TIDE score. K. The percentage of immunotherapy responders and non-responders in high and low CDI group using TIDE score. L. The difference of TMB between high and low CDI group. M. The Kaplan-Meier survival curve showed the relationship between OS and CDI in HNSCC patients receiving immunotherapy. N. The percentage of immunotherapy responders and non-responders in high and low CDI group in HNSCC patients receiving immunotherapy. O. The difference of CDI between immunotherapy responders and non-responders. P. The relationship of CDI, MHC, EC, SC and IPS in the TCGA cohort. Q-T. The difference of IPS between high and low CDI group.

high and low CDI group using TIDE score (**Figure 4K**). As higher tumor mutation burden (TMB) take the vital involvement in stronger antitumor immune response [31], TMB in each patient was calculated and the difference of TMB between high and low CDI groups was analyzed in **Figure 4L**. The results suggested that the TMB in low CDI group was lower than that of high CDI group. Next, we further investigated the relationship of prognosis in HNSCC patients receiving immunotherapy in IMvigor 210 cohort with CDI signature. The Kaplan-Meier survival curve showed that overall survival of low CDI group was higher compared to high CDI group (P<0.039) (**Figure 4M**). The percentage of immunotherapy responders and non-responders in high and low CDI group in HNSCC patients receiving immunotherapy as well as the difference of CDI between immunotherapy responders and non-responders was compared in **Figure 4N** and **4O**, respectively. Taken together, we inferred that low CDI group benefit more from immunotherapy, supporting the above conclusion. Furthermore, we explored the correlation of CDI with immunotherapy related biomarkers including MHC molecular (MHC), effector cells (EC), immune checkpoints (CP) and immunosuppressive cells (SC). Among them, MHC and EC promoted anti-tumor immune response while CP and SC suppresses anti-tumor immune response. The analogous result was also observed in **Figure 4P** that the CDI was negatively linked with the expression of EC and MHC while positively linked with the expression of CP and SC. Although immune cell proportion score (IPS) between high and low CDI group had no significance (P = 0.29), the relative probability to immune checkpoint inhibitor including anti PD1/PDL1/PDL2, anti-CTLA4 and both treatment in low CDI group was higher (P<0.05) (**Figure 4Q-T**).

Gene set enrichment analysis and evaluation of drug efficacy of the CDI signature

Due to the intense relationship between the CDI signature and prognosis, immune microenvironment, and immunotherapy response of HNSCC, our aim was to apply gene set enrichment analysis to explore their biological process and internal connection. Using KEGG functional enrichment analysis, we found that the DEGs between high and low CDI populations were distinctively enriched in 15 KEGG pathways (P<0.05). Among them, KEGG RETINAL METABOLISM, GLUTATHIONE METABOLISM, BIOSYNTHESIS LACTO AND NOTCHED SERIES, GLYCOLYSIS GLUCONEOGENESIS, RIBOFLAVIN METABOLISM, GLYCOSAMINOGLYCAN BIOSYNTHESIS CHONDROITIN SLUFATE, ADHERENS JUNCTION, CELL CYCLE, ECM RECEPTOR INTERACTION, NOTCH SIGNALLING PATHWAY, and GAP JUCTION were abundant in high CDI group and the low-CDI group had the most significant way in KEGG LINOLEIC ACID METABLOSIM, ARACHIDONIC ACID METABOLISM, PHENYLALANINE METABOLISM, TAURINE AND HYPOTAUINE METABOLISM (Figure S4A). To explore the relationship of tumor related biological processes with CDI signature, Gene Set Enrichment Analysis (GSEA) was performed. As shown in Figure S4B, a total of 15 hallmark gene sets were enriched (P<0.05). Hallmarks (including P53 PATHWAY, REACTIVE OXYGEN SPECIES PATHWAY, NECROPTOSIS, NOTCH SIGNALLING, WNT BETA CATEMIN SIGNALLING, EPITHELIAL MESENCHYMAL TRANSITION, TGF BETA SIGNALLING, HEDGEHOG SIGNALLING, G2M CHECKPOINT, ANGIOGENESIS, E2F TARGETS, DNA REPAIR, CUPROPTOSIS) were closely related with high CDI, indicating that the activation of these biological processes may play the vital role in tumorigenesis and progression. In contrast, the other hallmarks (KRAS SIGNALLING DN, PYROPTOSIS) were related with low CDI, implying that their activation participated in the tumor suppression and prolonged prognosis in HNSCC patients.

High-resolution scRNA-seq revealed the immune landscape of HNSCC

To characterize the immune landscape in HNSCC, tumor tissue samples from 6 patients with HNSCC were reclustered and annotated. All immune cells were classified into 13 cell types based on the expression level of canonical marker genes as reported previously using the dimensional reduction method which was called t-distributed stochastic neighbor embedding (t-SNE), including memory B cells, naïve B cells, memory CD4+ T cells, naïve CD4 T cells, memory CD8+ T cells, naïve CD8+ T cells, regulatory T cells (Tregs), macrophages (M), dendritic cells (DC), natural killer cells (NK), granulocytes (Gran), mast cells and unidentified cells

by well-recognized gene markers (**Figure 5A**). Next, we investigated the fraction of immune cell types in different clusters (**Figure 5B**). The results suggested that different immune cell types varied significantly among different clusters. To be specific, naïve CD4+ T cells were prevalent in C1-C5, memory CD8+ T cells were predominant in C2-C4, while naïve B cells were abundant in C6. Using t-SNE analysis, CD4+/CD8+ T cells were categorized as memory and naïve CD4+/CD8 T cells. It was revealed in the development trajectory analyses of CD4+/CD8+ T cells that a similar trajectory between different pseudotime, Seurat clusters, state, and cell subtypes. Furthermore, multiple branched structures was divided into 3 branches: the naïve or effector cells as root extended to Tregs, memory and exhausted cells as diverse end states of a branch, which was in agreement with previous studies (**Figure 5C-L**).

Cell communication network analysis in HNSCC

To further illustrate the mechanism that immune cell exposed the regulatory effects in tumorigenesis, we investigated the interaction among multiple of immune cells through specific signaling pathway. The number of interactions or interaction weights/strength among immune cell types was described in Figure S5A, S5B. As shown in Figure S5C-F, the interaction number and weights/strength of memory or naïve CD8+ T cells with other immune cell types was deeper explored. The memory and naïve CD8+ T cells was strongly linked with M1 and naïve B cells, respectively in the interaction number. The memory and naïve CD8+ T cells was highly related with macrophages and M2 cells, respectively in the interaction weights/strength. Furthermore, the role of related signaling pathways in cell-cell interaction was in depth studied. We found that the interaction between immune cells was closely associated with three important pathway in executive function processes. Notably, activation of the MIF pathway was accompanied by high intensity interaction of multiple immune cells, especially memory CD8+ T cells, which played an important role in signaling network including CXCL and IL16. In addition, we also noted that the interaction of M2 macrophages in three key pathway networks was not significant, which might be related to its pro-tumor immune function (Figure S5G-L). Signaling input, output and transmission of signaling pathway constitute the signaling interaction network. The contribution weight of outgoing and incoming signaling patterns to immune cell types in cell communication network system was also shown in Figure S5M, S5N. For example, memory CD8+ T cells are most likely to interact with other cells by inputting GELACTIN signaling and outputting CCL and INFII signaling, thus exerting effector functions in antitumor immune response.

Biological functions of CAAP1 and BCL2L2-PABPN

To ascertain the efficacy of the apoptosis signature, we examined CAAP1 and BCL2L2-PABPN, primary contributors to intrinsic and extrinsic apoptosis-related risk models, respectively. Our initial investigation focused on measuring the expression levels of CAAP1 and BCL2L2-PABPN in HNSCC cell lines, revealing higher expression of both CAAP1 and BCL2L2-PABPN in tumor tissues (T) as compared to matched adjacent non-tumor tissues (N) (**Figure 6A**, left). We also endeavored to ascertain the expression levels of CAAP1 and BCL2L2-PABPN across various HNSCC cell lines (**Figure 6B**, right). In a further phase of our study, we knocked out CAAP1 and BCL2L2-PABPN in Fadu and HN8 cell lines, respectively (**Figure 6C**). Subsequent wound healing and transwell assays reveal a significant suppression of cellular migration following the loss of CAAP1 and BCL2L2-PABPN (**Figure 6D**, **6E**).

Chemotherapy primarily exerts anti-tumor effects by inducing cell death. ABT-737, a recognized inducer of intrinsic apoptosis, was administered at a concentration of 30 μM for 24 hours, aligning with dosages employed in prior investigations on HeLa cells [32]. The application of ABT-737 led to the heightened cleavage of intrinsic apoptosis-associated proteins, specifically caspase 9 in Fadu cells. Intriguingly, CAAP1 knockout further enhanced ABT-737-induced intrinsic apoptosis (**Figure 7A-D**). To elucidate the pathways through which ABT-737 induces apoptosis in Fadu cells, we analyzed the activation of caspase cleavage cascades, assessing downstream mediators of cellular apoptosis through immunoblotting. The caspase 9 cleavage events was shown in Fadu cell

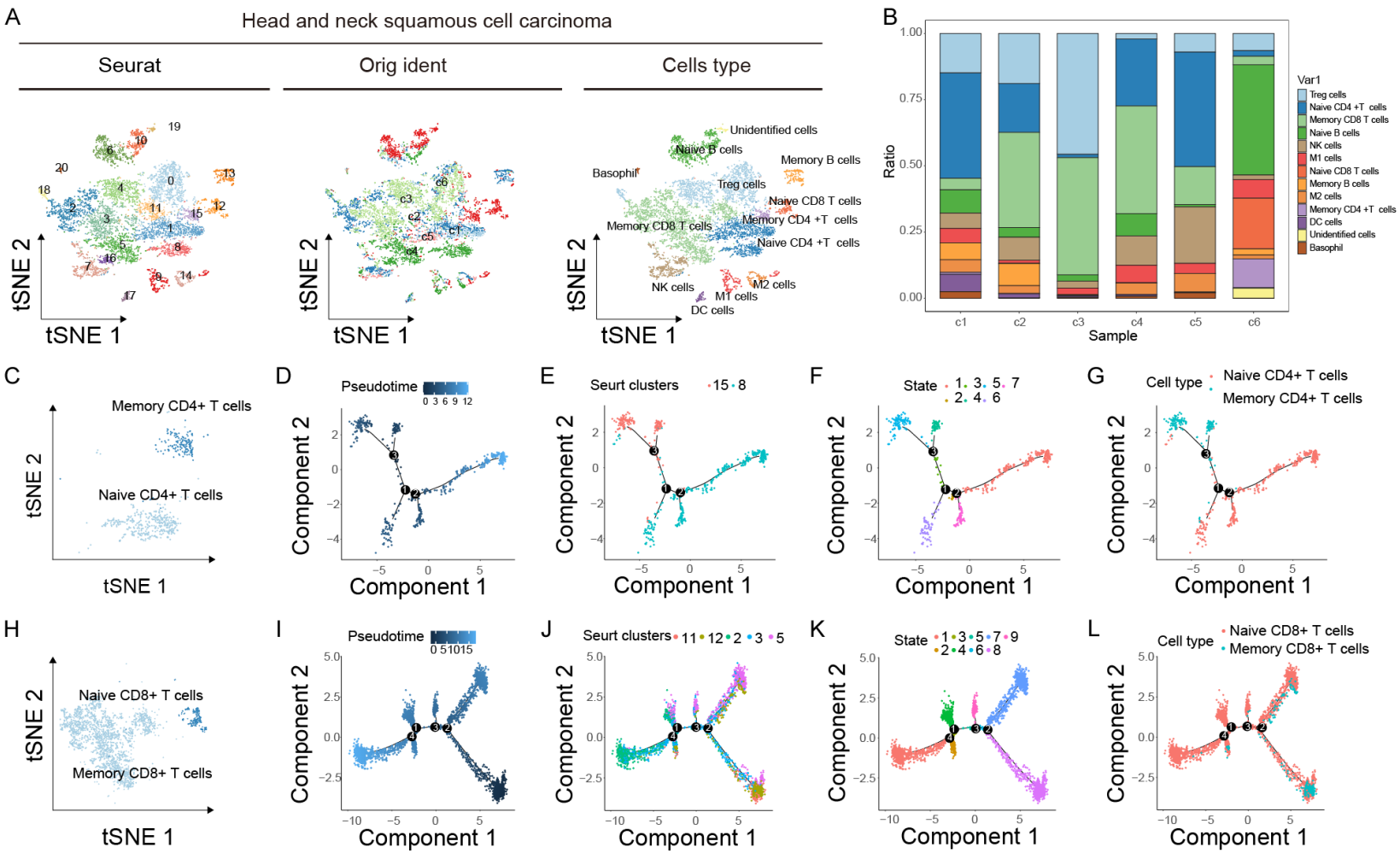

Figure 5. High-resolution immune cell-type landscape of HNSCC samples. A. t-SNE plot showing the identified cell types of all immune cells. B. Fraction of cell types originating from each sample. C-G. Developmental trajectory of CD4+ T cells inferred by monocle, colored by pseudotime, Seurat clusters, state, and cell subtype. H-L. Developmental trajectory of CD8+ T cells inferred by monocle, colored by pseudotime, Seurat clusters, state, and cell subtype.

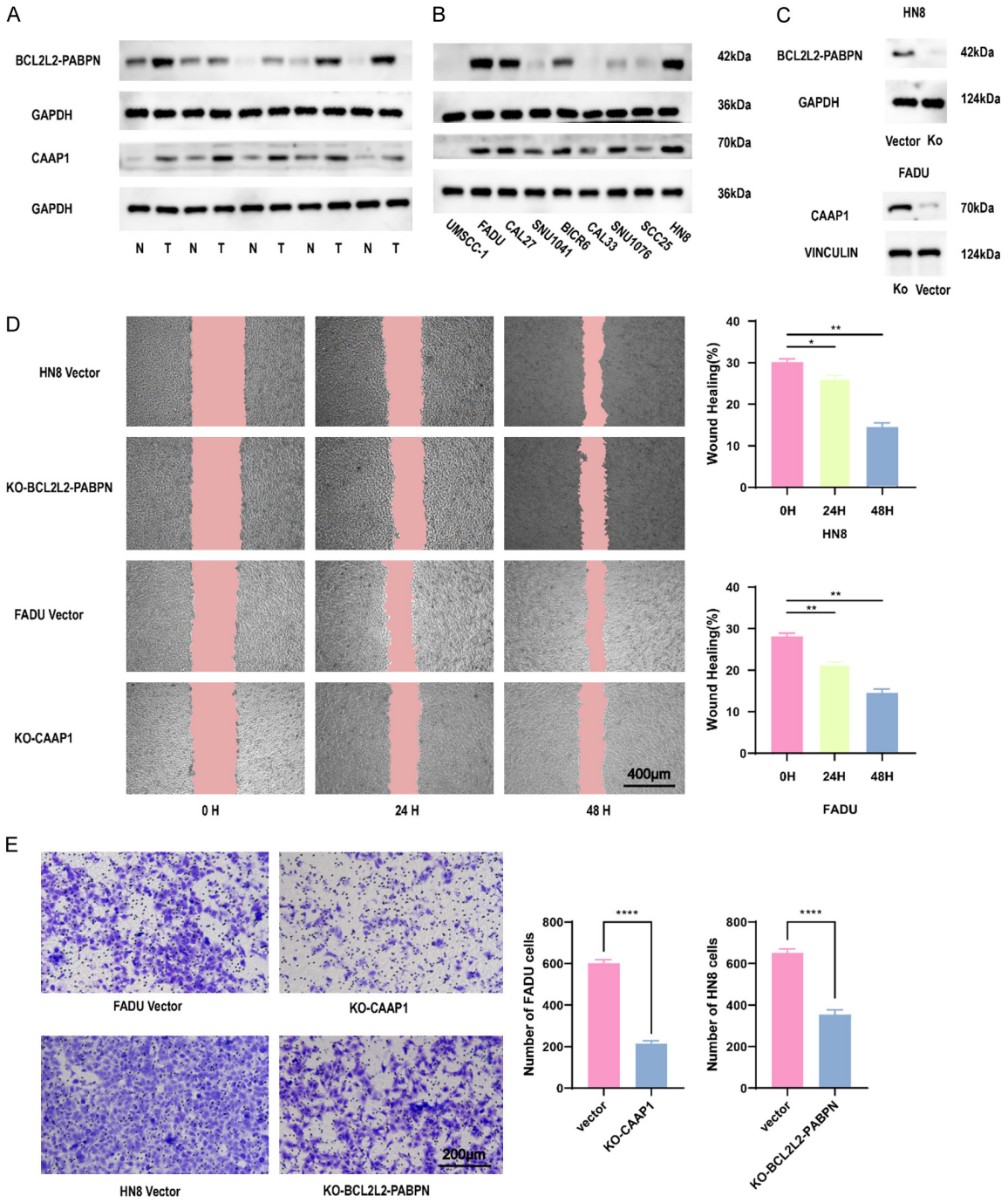

Figure 6. CAAP1 and BCL2L2-PABPN can promote cellular proliferation. (A) Western blot analysis of total cell lysates of HNSCC cell lines demonstrates the expression of CAAP1 and BCL2L2-PABPN. (B) CAAP1 and BCL2L2-PABPN expressions in five paired tumor tissues (T) and their adjacent normal tissues (N). (C) The expression of CAAP1 and BCL2L2-PABPN in FADU and HN8 cells respectively after transferring with sgRNA. Knockdown of CAAP1 and BCL2L2-PABPN inhibited the Invasion and migration of HNSCC cells were test by wound-healing assay (D), transwell assay (E).

with or without CAAP1-knockout. Bax, a marker for intrinsic apoptosis, was scrutinized for its activity in Fadu cells during ABT-737 exposure, showing decreased levels (**Figure 7E**).

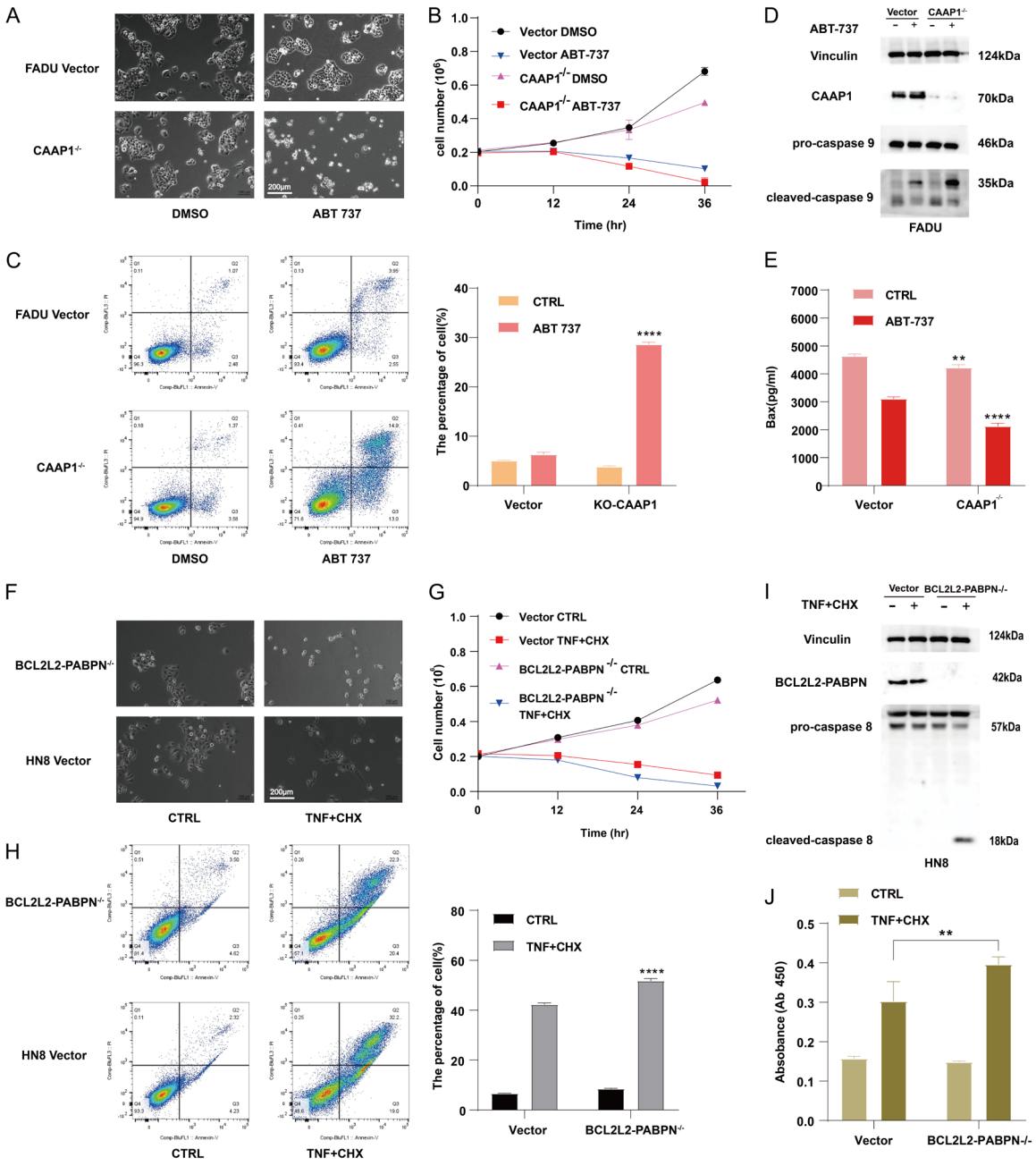

Figure 7. CAAP1 inhibit HNSCC intrinsic apoptosis, BCL2L2-PABPN inhibit HNSCC extrinsic apoptosis. (A) Phase-contrast photomicrographs showing Fadu cells treated with ABT-737 for 12 h, analysis with Cell Counting Kit CCK-8 assay (B). (C) Fadu and CAAP1-/- cells were treated with ABT-737 for 10 h, and then stained with Annexin V-FITC and analysed by flow cytometry; Percentage of apoptotic cells was measured right. (D) Western blot of full-length and cleaved caspase 9 for Fadu cell lines treated with ABT-737 (30 μM) for 12 h, (E) Bax level as measured using EIA assay. (F) Cells were photographed 24 h after drug treatment and analysis by CCK8 (G). (H) HN8 and BCL2L2-PABPN-/- cells were treated with TNF-α/CHX for 12 h, and then stained with Annexin V-FITC and analysed by flow cytometry; Percentage of apoptotic cells was measured right. CTRL, control. (I) Western blot of HN8 and BCL2L2-PABPN-/- cell lines treated with TNF-α and cycloheximide (CHX) for 12 h. TNF-α (5 ng/ml), CHX (20 ug/ml). (J) Caspase 8 activity as measured using enzymatic assay and represented by optical density at 450 nm (OD450).

Previous investigations have demonstrated that TNFα, combined with cycloheximide (CHX), can induce extrinsic apoptosis. Drawing upon concentrations delineated in the published lit-

erature [33], we selected CHX at 20 μg/ml and TNF-α at 5 ng/ml to validate this form of apoptosis (**Figure 7F-H**). We observed an augmentation of caspase 8 cleavage and activity following the treatment with TNFα and CHX (**Figure 7I**, **7J**). The elimination of BCL2L2-PABPN significantly intensified TNFα/CHX-induced apoptosis (**Figure 7H-J**).

CAAP1 has been identified as an inhibitor of Caspase3/8/9/10 activity [34] and its knockout has been shown to enhance apoptosis and impede the progression of gastric and liver cancers [35]. Additionally, research by Anderson et al revealed that CAAP1-mediated apoptosis operates through the mitochondrial pathway [34]. Similarly, the knockdown of BCL2L2-PABPN1 in U87 and U251 cells facilitated cell death [36], corroborating our conclusion. Furthermore, our results align with study showing overexpression of BCL2L2-PABPN1 in bladder cancer [37].

Absence of CAAP1 enhances antitumor immunity and reduces the growth of HNSCC

Our research has demonstrated that both intrinsic and extrinsic apoptosis pathways play roles in inhibiting tumor progression in HNSCC. Specifically, CAAP1 is implicated in the intrinsic apoptosis pathway of HNSCC cells, while BCL2L2-PABPN1 plays a role in extrinsic apoptosis. Phenotypic analyses revealed that knocking out CAAP1 has a more pronounced pro-apoptotic and anti-tumor effects compared to the deletion of BCL2L2-PABPN1. Consequently, we focused on our animal studies on the intrinsic apoptosis pathway involving CAAP1.

To explore whether the silencing CAAP1 contributes to an anticancer phenotype *in vivo*, we conducted several experiments. Fadu cells with and without CAAP1 gene knockout were subcutaneously implanted (**Figure 8A**). Our observations revealed that CAAP1 depletion significantly inhibited tumors growth in nude mice (**Figure 8B-D**). Furthermore, we implanted CAAP1-deficient Meer cells subcutaneously in C57BL/6 mice, and compared to immunodeficient nude mice, the difference in tumor growth was more pronounced in immunocompetent mice (**Figure 8E-G**). This suggests that the absence of CAAP1 triggers a more robust antitumor immune response in the context of a complete immune system. Compared to the control group, tumors in the CAAP1-deficient group were smaller (**Figure 8F**, **8G**) and the expression of pro-apoptotic proteins Bax and Bak were increased (**Figure 8H**), indicating enhanced tumor cell apoptosis. Additionally, we assessed the immune response by analyzing the infiltration of immune cells in tumor tissues. Flow cytometry was employed to separately evaluate the quantity and activity (GZMB+) of CD8+ T cells in tumor tissues and blood. In the CAAP1-deficient group, the number of CD8+ T cells in both blood (**Figure 8I**) and tumor tissue (**Figure 8J**) was significantly higher than that in the control group, which further support the difference in tumorigenesis. Meanwhile, we found that the number of GZMB+CD8+ T cells in blood was notably increased in CAAP1 deficient group compared to control group (**Figure 8K**). These results suggest that the loss of CAAP1 contributes to tumor suppression not only by inducing tumor cell apoptosis but also by enhancing CD8+ T cell activation.

Discussion

Our study represents the first comprehensive analysis of 15 types of cell death patterns, establishing the CDI signature using the TCGA cohort, and validating its superior predictive performance using GSE27020 and GSE41613 datasets. We identified the correlation of the CDI signature with enriched pathways, immune modulators, immune cell infiltration as well as interaction.

Decades of research have linked various cell death processes to malignant tumor development and metastasis. Among these, apoptosis-regulating mechanisms have been extensively studied in multiple organisms over the last 30 years. Both intrinsic and extrinsic apoptosis pathways are crucial to various physiological and pathological processes, including cell homeostasis, tissue remodeling, and tumorigenesis. However, their mechanisms of action differ in a variety of tumors, including HNSCC. Specifically, intrinsic apoptosis, triggered by internal stresses such as DNA damage, oxidative stress, and oncogene activation, involves the release of cytochrome c from mitochondria. This leads to caspase-9 activation followed by the executioner caspases. Intrinsic

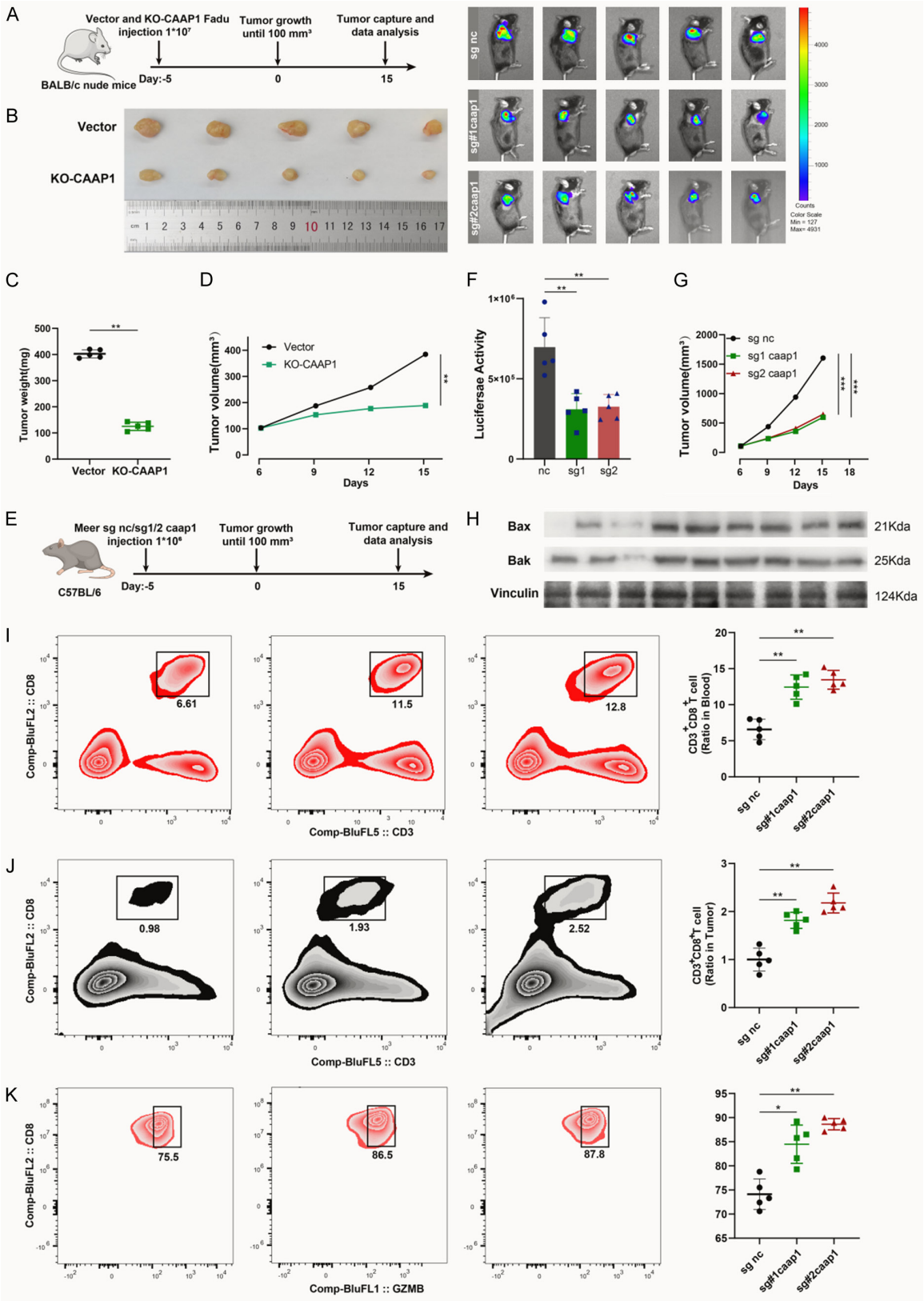

Figure 8. In immune-competent mouse models, inhibition of CAAP1 induces antitumor immunity. (A) A schematic view of the treatment plan. (B) Tumor bodies dissected 15 days after tumor formation in BLAB/C nude mice. (C, D) Summary of tumor weight (C) and volume data (D) of Fadu tumors harvested after euthanizing the mice. (E) A sche-

matic view of the treatment plan and C57 mice received GFP-Luc sg nc, or sg caap1 meer cells were injected with luciferin. (F, G) Summary of luciferase activity (F) and volume data (G) of meer tumors harvested after euthanizing the mice. (H) Differences in the expression of CAAP1, Bax, and Bak in tumor tissues among different groups. (I-K) FACS of CD8+ in CD3+ cells and GZMB+CD8+ in CD3+ TILs from sg nc, or sg caap1 meer xenografts and quantification.

apoptosis is often suppressed in HNSCC due to mutations in tumor suppressor genes or the overexpression of anti-apoptotic proteins like Bcl-2, rendering the tumor resistant to certain chemotherapeutic drugs [37]. Externally, signals such as FasL or TNF-α bind to death receptors on the cell surface, initiating extrinsic apoptosis. This process leads to the formation of the death-inducing signaling complex and the activation of caspase-8. However, it can be compromised due to alterations in death receptor expression or disruptions in downstream signaling, impacting immune-mediated cell death [15]. We constructed a signature of 25 CDI-related genes, which was proved as a promising predictor of HNSCC prognosis. It's worth noting that 10 of these genes including KRT18, PPARG, CTLA4, IKBKB, STK11, NPM1, APP, MAP3K5, BAK1, EPO were tightly associated with signature as shown in gene interaction network.

A recent study identified PPARG as a potential pretreatment predictive biomarker in HNSCC patients treated with neoadjuvant nivolumab [38]. This was because that PPARγ served to adaptively temper COX-2-mediated inflammation, contributing to the progression and development of HNSCC [39]. CTLA4, tightly associated with a worse prognosis in HNSCC, acted as a negative regulator of T-cell activation, leading to more aggressive biologic subtypes and therefore promoting tumor progression. IKBKB encodes a Ser/Thr kinase, which phosphorylates a wide range of substrates and regulates various cellular process including cell cycle, metabolism, and differentiation [40]. Its significance was underscored in a seven-gene signature predicting the prognosis of HNSCC [41]. STK11 plays a crucial role in a number of cancer types, including HNSCC, where its reduced expression levels could be partly explained by the negative regulation of miR-100-3p [42], corroborated by our study. A previous study reported that the EPO gene promoted tumor growth and prevented apoptosis by encoding a secreted glycoprotein hormone. It was postulated that heightened expression of EPO attenuated tumor growth by exerting the deleterious effects of hypoxia on tumor growth, metastasis, and treatment resistance [43, 44]. Alterations in the expressions of BAK1 in HNSCC, which play a pivotal role in cell cycle regulation, apoptotic modes and angiogenesis, was also noted [45, 46]. Additionally, a reduction in NPM1 mRNA, which codes for the proteins that regulate the p53 activity, was observed after application of radiotherapy [47]. We addressed the hypothesis that NAE1/APP-BP1 expression levels influencd p53 activity and cell survival upon ionizing irradiation. Cancer cells expressing NAE1/APP-BP1 exhibited decreased sensitivity to ionizing radiation, altering transcriptional activity driven by p53 [48], which was consistent with our findings. Moreover, the expression of MAP3K5, known as apoptosis signal-regulating kinase 1 (ASK1), was significantly reduced in HNSCC tissues compared to adjacent non-tumor tissue [49].

During tumor progression, cancer cells can survive because of the immunosuppressive tumor microenvironment, which allows them to escape immune surveillance and resist drug interference [50]. In theory, high CDI groups exhibit reduced levels of immune cell infiltration, immune checkpoints and other immunotherapy related biomarkers, suggesting compromised immune functions [51, 52]. In our study, the analysis of immune cells infiltration revealed that CD8+ T cells, naïve B cells, CD4+ memory activated T cells, follicular helper T cells, and Tregs had higher infiltration rates in the low CDI group. Conversely, M2 macrophages and CD4 memory resting T cells had higher infiltration in the high CDI group of HNSCC patients, supporting above assumptions. Numerous studies have associated dense T cell infiltration, especially T cells CD8, with favorable prognoses in cancer [53, 54]. M0 cells, also named resting macrophages, are polarized into either pro-inflammatory M1 or anti-inflammatory M2 phenotypes, further influence outcomes. Previous studies indicated that an abundance of M1 macrophages typically indicates better outcome, while an enrichment of M2 macrophages suggests a worse outcome in HNSCC microenvironment [55].

In addition to immune cells infiltration, we also investigated immunotherapy-related biomarkers in high and low CDI groups. Immunotherapy has emerged as an effective treatment for many cancers, including HNSCC. Nevertheless, searching for the optimal population who benefits from immunotherapy remains challenging [56, 57]. Tumor mutation burden (TMB) refers to the number of somatic mutations without germline mutations in tumor genome. We found the high CDI group in HNSCC had elevated levels of TMB. Although higher TMB may contribute to the better immunotherapy response [58], the increased TMB predicted increasingly poor prognosis, aligning with our results. Additionally, higher levels of immune checkpoints, including LAG3, and PDCD1, CTLA4, were observed in low CDI group, demonstrating these patients might be benefit more from immunotherapy. Our study also explored the relationship between TIDE score, MHC molecular (MHC), effector cells (EC), immune checkpoints (CP) and immunosuppressive cells (SC) with CDI signature. This analysis confirmed that a low CDI was a predictor of stronger immune response. Furthermore, through single-cell analysis, we provided a comprehensive picture of the HNSCC immune landscape, highlighting the characteristics of immune cell subtype, cell-cell interaction, and key signaling transduction pathways.

To obtain more information from the model that can benefit patients, we selected two genes with higher weight coefficients in the two death modes used to construct the model. These genes were then the focus of our in vitro and in vivo experiments. Surprisingly, we found that the loss of CAAP1 not only induced increased apoptosis but also enhanced antitumor immunity. This finding provides an important reference for developing targeted drugs for head and neck cancer. However, this conclusion is currently limited to animal models, and further research is needed to elucidate the specific mechanism by which CAAP1 deficiency influences tumor suppression. In summary, the establishment of this model provides a comprehensive framework for identifying high-risk patients or immunotherapy-sensitive patients clinically, and the discovery of CAAP1 provides a new direction for future research.

Although the prognostic model exhibited excellent predictive performance, our study had certain limitations. The incomplete clinicopathological information from TCGA and GEO databases means that the CDI might not be independent predictor of HNSCC prognosis. Additionally, the predictivity of CDI signature was primarily validated using GEO database, necessitating further confirmation in multicenter randomized controlled trials with larger and more diverse populations.

In conclusion, the CDI signature established in this study serves as a novel prognostic predictor for HNSCC patients, significantly enhancing clinical outcome assessments.

Acknowledgements

We would like show sincere appreciation to the editors and reviewers for critical comments on this article. This study was supported by Natural Science Foundation of Hunan Province (2023JJ50508), Loudi Science and Technology Bureau ([2022]32) and Loudi Science and Technology Bureau ([2023]35).

Disclosure of conflict of interest

None.

Address correspondence to: Dr. Fusen Peng and Ying Zhang, Department of Otolaryngology Head and Neck Surgery, Loudi Central Hospital, Loudi 417011, Hunan, The People's Republic of China. E-mail: FusenPeng81@163.com (FSP); 67344044@qq.com (YZ)

References

[1] Miller KD, Nogueira L, Devasia T, Mariotto AB, Yabroff KR, Jemal A, Kramer J and Siegel RL. Cancer treatment and survivorship statistics, 2022. CA Cancer J Clin 2022; 72: 409-436.

[2] Jemal A, Siegel R, Ward E, Murray T, Xu J and Thun MJ. Cancer statistics, 2007. CA Cancer J Clin 2007; 57: 43-66.

[3] Giraldi L, Leoncini E, Pastorino R, Wünsch-Filho V, de Carvalho M, Lopez R, Cadoni G, Arzani D, Petrelli L, Matsuo K, Bosetti C, La Vecchia C, Garavello W, Polesel J, Serraino D, Simonato L, Canova C, Richiardi L, Boffetta P, Hashibe M, Lee YCA and Boccia S. Alcohol and cigarette consumption predict mortality in patients with head and neck cancer: a pooled analysis within the International Head and Neck Cancer Epidemiology (INHANCE) Consortium. Ann Oncol 2017; 28: 2843-2851.

[4] Van den Bossche V, Zaryouh H, Vara-Messler M, Vignau J, Machiels JP, Wouters A, Schmitz S

and Corbet C. Microenvironment-driven intratumoral heterogeneity in head and neck cancers: clinical challenges and opportunities for precision medicine. Drug Resist Updat 2022; 60: 100806.
[5] Leemans CR, Braakhuis BJ and Brakenhoff RH. The molecular biology of head and neck cancer. Nat Rev Cancer 2011; 11: 9-22.
[6] Petit C, Lacas B, Pignon JP, Le QT, Grégoire V, Grau C, Hackshaw A, Zackrisson B, Parmar MKB, Lee JW, Ghi MG, Sanguineti G, Temam S, Cheugoua-Zanetsie M, O'Sullivan B, Posner MR, Vokes EE, Cruz Hernandez JJ, Szutkowski Z, Lartigau E, Budach V, Suwiński R, Poulsen M, Kumar S, Ghosh Laskar S, Mazeron JJ, Jeremic B, Simes J, Zhong LP, Overgaard J, Fortpied C, Torres-Saavedra P, Bourhis J, Aupérin A and Blanchard P; MACH-NC and MARCH Collaborative Groups. Chemotherapy and radiotherapy in locally advanced head and neck cancer: an individual patient data network meta-analysis. Lancet Oncol 2021; 22: 727-736.
[7] Raudenská M, Balvan J and Masařík M. Cell death in head and neck cancer pathogenesis and treatment. Cell Death Dis 2021; 12: 192.
[8] Huang G and Pan ST. ROS-mediated therapeutic strategy in chemo-/radiotherapy of head and neck cancer. Oxid Med Cell Longev 2020; 2020: 5047987.
[9] Sannigrahi MK, Singh V, Sharma R, Panda NK and Khullar M. Role of autophagy in head and neck cancer and therapeutic resistance. Oral Dis 2015; 21: 283-291.
[10] Chen X, Zeh HJ, Kang R, Kroemer G and Tang D. Cell death in pancreatic cancer: from pathogenesis to therapy. Nat Rev Gastroenterol Hepatol 2021; 18: 804-823.
[11] Galluzzi L, Vitale I, Aaronson SA, Abrams JM, Adam D, Agostinis P, Alnemri ES, Altucci L, Amelio I, Andrews DW, Annicchiarico-Petruzzelli M, Antonov AV, Arama E, Baehrecke EH, Barlev NA, Bazan NG, Bernassola F, Bertrand MJM, Bianchi K, Blagosklonny MV, Blomgren K, Borner C, Boya P, Brenner C, Campanella M, Candi E, Carmona-Gutierrez D, Cecconi F, Chan FK, Chandel NS, Cheng EH, Chipuk JE, Cidlowski JA, Ciechanover A, Cohen GM, Conrad M, Cubillos-Ruiz JR, Czabotar PE, D'Angiolella V, Dawson TM, Dawson VL, De Laurenzi V, De Maria R, Debatin KM, DeBerardinis RJ, Deshmukh M, Di Daniele N, Di Virgilio F, Dixit VM, Dixon SJ, Duckett CS, Dynlacht BD, El-Deiry WS, Elrod JW, Fimia GM, Fulda S, García-Sáez AJ, Garg AD, Garrido C, Gavathiotis E, Golstein P, Gottlieb E, Green DR, Greene LA, Gronemeyer H, Gross A, Hajnoczky G, Hardwick JM, Harris IS, Hengartner MO, Hetz C, Ichijo H, Jäättelä M, Joseph B, Jost PJ, Juin PP, Kaiser WJ, Karin M, Kaufmann T, Kepp O, Kimchi A, Kitsis RN, Klionsky DJ, Knight RA, Kumar S, Lee SW, Lemasters JJ, Levine B, Linkermann A, Lipton SA, Lockshin RA, López-Otín C, Lowe SW, Luedde T, Lugli E, MacFarlane M, Madeo F, Malewicz M, Malorni W, Manic G, Marine JC, Martin SJ, Martinou JC, Medema JP, Mehlen P, Meier P, Melino S, Miao EA, Molkentin JD, Moll UM, Muñoz-Pinedo C, Nagata S, Nuñez G, Oberst A, Oren M, Overholtzer M, Pagano M, Panaretakis T, Pasparakis M, Penninger JM, Pereira DM, Pervaiz S, Peter ME, Piacentini M, Pinton P, Prehn JHM, Puthalakath H, Rabinovich GA, Rehm M, Rizzuto R, Rodrigues CMP, Rubinsztein DC, Rudel T, Ryan KM, Sayan E, Scorrano L, Shao F, Shi Y, Silke J, Simon HU, Sistigu A, Stockwell BR, Strasser A, Szabadkai G, Tait SWG, Tang D, Tavernarakis N, Thorburn A, Tsujimoto Y, Turk B, Vanden Berghe T, Vandenabeele P, Vander Heiden MG, Villunger A, Virgin HW, Vousden KH, Vucic D, Wagner EF, Walczak H, Wallach D, Wang Y, Wells JA, Wood W, Yuan J, Zakeri Z, Zhivotovsky B, Zitvogel L, Melino G and Kroemer G. Molecular mechanisms of cell death: recommendations of the nomenclature committee on cell death 2018. Cell Death Differ 2018; 25: 486-541.
[12] Tang D, Kang R, Berghe TV, Vandenabeele P and Kroemer G. The molecular machinery of regulated cell death. Cell Res 2019; 29: 347-364.
[13] Yuan L, Li P, Zheng Q, Wang H and Xiao H. The ubiquitin-proteasome system in apoptosis and apoptotic cell clearance. Front Cell Dev Biol 2022; 10: 914288.
[14] He S, Chakraborty R and Ranganathan S. Proliferation and apoptosis pathways and factors in oral squamous cell carcinoma. Int J Mol Sci 2022; 23: 1562.
[15] Xue Y, Jiang X, Wang J, Zong Y, Yuan Z, Miao S and Mao X. Effect of regulatory cell death on the occurrence and development of head and neck squamous cell carcinoma. Biomark Res 2023; 11: 2.
[16] Nisar S, Yousuf P, Masoodi T, Wani NA, Hashem S, Singh M, Sageena G, Mishra D, Kumar R, Haris M, Bhat AA and Macha MA. Chemokine-cytokine networks in the head and neck tumor microenvironment. Int J Mol Sci 2021; 22: 4584.
[17] Bredesen DE, Mehlen P and Rabizadeh S. Apoptosis and dependence receptors: a molecular basis for cellular addiction. Physiol Rev 2004; 84: 411-430.
[18] Schulze-Osthoff K, Ferrari D, Los M, Wesselborg S and Peter ME. Apoptosis signaling by death receptors. Eur J Biochem 1998; 254: 439-459.

[19] Chipuk JE, Bouchier-Hayes L and Green DR. Mitochondrial outer membrane permeabilization during apoptosis: the innocent bystander scenario. Cell Death Differ 2006; 13: 1396-1402.
[20] Shen YQ, Guerra-Librero A, Fernandez-Gil BI, Florido J, García-López S, Martinez-Ruiz L, Mendivil-Perez M, Soto-Mercado V, Acuña-Castroviejo D, Ortega-Arellano H, Carriel V, Diaz-Casado ME, Reiter RJ, Rusanova I, Nieto A, López LC and Escames G. Combination of melatonin and rapamycin for head and neck cancer therapy: suppression of AKT/mTOR pathway activation, and activation of mitophagy and apoptosis via mitochondrial function regulation. J Pineal Res 2018; 64.
[21] Ow TJ, Thomas C, Fulcher CD, Chen J, López A, Reyna DE, Prystowsky MB, Smith RV, Schiff BA, Rosenblatt G, Belbin TJ, Harris TM, Childs GC, Kawachi N, Schlecht NF and Gavathiotis E. Apoptosis signaling molecules as treatment targets in head and neck squamous cell carcinoma. Laryngoscope 2020; 130: 2643-2649.
[22] Niyomtham N, Koontongkaew S, Yingyongnarongkul BE and Utispan K. Apis mellifera propolis enhances apoptosis and invasion inhibition in head and neck cancer cells. PeerJ 2021; 9: e12139.
[23] Uzunparmak B, Gao M, Lindemann A, Erikson K, Wang L, Lin E, Frank SJ, Gleber-Netto FO, Zhao M, Skinner HD, Newton J, Sikora AG, Myers JN and Pickering CR. Caspase-8 loss radiosensitizes head and neck squamous cell carcinoma to SMAC mimetic-induced necroptosis. JCI Insight 2020; 5: e139837.
[24] Lee J, You JH, Kim MS and Roh JL. Epigenetic reprogramming of epithelial-mesenchymal transition promotes ferroptosis of head and neck cancer. Redox Biol 2020; 37: 101697.
[25] Cai J, Yi M, Tan Y, Li X, Li G, Zeng Z, Xiong W and Xiang B. Natural product triptolide induces GSDME-mediated pyroptosis in head and neck cancer through suppressing mitochondrial hexokinase-II. J Exp Clin Cancer Res 2021; 40: 190.
[26] Li T, Fu J, Zeng Z, Cohen D, Li J, Chen Q, Li B and Liu XS. TIMER2.0 for analysis of tumor-infiltrating immune cells. Nucleic Acids Res 2020; 48: W509-W514.
[27] Becht E, Giraldo NA, Lacroix L, Buttard B, Elarouci N, Petitprez F, Selves J, Laurent-Puig P, Sautès-Fridman C, Fridman WH and de Reyniès A. Estimating the population abundance of tissue-infiltrating immune and stromal cell populations using gene expression. Genome Biol 2016; 17: 218.
[28] Newman AM, Liu CL, Green MR, Gentles AJ, Feng W, Xu Y, Hoang CD, Diehn M and Alizadeh AA. Robust enumeration of cell subsets from tissue expression profiles. Nat Methods 2015; 12: 453-457.
[29] Yoshihara K, Shahmoradgoli M, Martinez E, Vegesna R, Kim H, Torres-Garcia W, Trevino V, Shen H, Laird PW, Levine DA, Carter SL, Getz G, Stemke-Hale K, Mills GB and Verhaak RG. Inferring tumour purity and stromal and immune cell admixture from expression data. Nat Commun 2013; 4: 2612.
[30] Cohen EEW, Bell RB, Bifulco CB, Burtness B, Gillison ML, Harrington KJ, Le QT, Lee NY, Leidner R, Lewis RL, Licitra L, Mehanna H, Mell LK, Raben A, Sikora AG, Uppaluri R, Whitworth F, Zandberg DP and Ferris RL. The Society for Immunotherapy of Cancer consensus statement on immunotherapy for the treatment of squamous cell carcinoma of the head and neck (HNSCC). J Immunother Cancer 2019; 7: 184.
[31] Zhang L, Li B, Peng Y, Wu F, Li Q, Lin Z, Xie S, Xiao L, Lin X, Ou Z, Cai T, Rong H, Fan S and Li J. The prognostic value of TMB and the relationship between TMB and immune infiltration in head and neck squamous cell carcinoma: a gene expression-based study. Oral Oncol 2020; 110: 104943.
[32] Galindo-Moreno J, Iurlaro R, El Mjiyad N, Diez-Perez J, Gabaldon T and Munoz-Pinedo C. Apolipoprotein L2 contains a BH3-like domain but it does not behave as a BH3-only protein. Cell Death Dis 2014; 5: e1275.
[33] Miura M, Friedlander RM and Yuan J. Tumor necrosis factor-induced apoptosis is mediated by a CrmA-sensitive cell death pathway. Proc Natl Acad Sci U S A 1995; 92: 8318-8322.
[34] Zhang Y, Johansson E, Miller ML, Jänicke RU, Ferguson DJ, Plas D, Meller J and Anderson MW. Identification of a conserved anti-apoptotic protein that modulates the mitochondrial apoptosis pathway. PLoS One 2011; 6: e25284.
[35] Zhang KX, Ding C, Liu QH and Zhu DM. Knockdown of LINC01087 inhibits gastric cancer malignant behavior by regulating the miR-135a-5p/CAAP1 axis. Funct Integr Genomics 2023; 23: 248.
[36] Zhang L, Wang D, Han X, Guo X, Cao Y, Xia Y and Gao D. Novel read-through fusion transcript Bcl2l2-Pabpn1 in glioblastoma cells. J Cell Mol Med 2022; 26: 4686-4697.
[37] Zhu D, Singh S, Chen X, Zheng Z, Huang J, Lin T and Li H. The landscape of chimeric RNAs in bladder urothelial carcinoma. Int J Biochem Cell Biol 2019; 110: 50-58.
[38] Liu S, Knochelmann HM, Lomeli SH, Hong A, Richardson M, Yang Z, Lim RJ, Wang Y, Dumitras C, Krysan K, Timmers C, Romeo MJ, Krieg C, O'Quinn EC, Horton JD, Dubinett SM, Paulos CM, Neskey DM and Lo RS. Response and re-

currence correlates in individuals treated with neoadjuvant anti-PD-1 therapy for resectable oral cavity squamous cell carcinoma. Cell Rep Med 2021; 2: 100411.
[39] Korbecki J, Bobinski R and Dutka M. Self-regulation of the inflammatory response by peroxisome proliferator-activated receptors. Inflamm Res 2019; 68: 443-458.
[40] Patel L, Pass I, Coxon P, Downes CP, Smith SA and Macphee CH. Tumor suppressor and anti-inflammatory actions of PPARgamma agonists are mediated via upregulation of PTEN. Curr Biol 2001; 11: 764-768.
[41] Page A, Navarro M, Suarez-Cabrera C, Bravo A and Ramirez A. Context-dependent role of IKKbeta in cancer. Genes (Basel) 2017; 8: 376.
[42] Ribeiro IP, Esteves L, Santos A, Barroso L, Marques F, Caramelo F, Melo JB and Carreira IM. A seven-gene signature to predict the prognosis of oral squamous cell carcinoma. Oncogene 2021; 40: 3859-3869.
[43] Yang D, Liu J, Liu N, Yin C, Zhang H and Xu J. The prognostic value of tumor mutational burden related 6-gene-based risk score in laryngeal cancer patients. BMC Oral Health 2022; 22: 510.
[44] Figueroa-Gonzalez G, Carrillo-Hernandez JF, Perez-Rodriguez I, Cantu de Leon D, Campos-Parra AD, Martinez-Gutierrez AD, Coronel-Hernandez J, Garcia-Castillo V, Lopez-Camarillo C, Peralta-Zaragoza O, Jacobo-Herrera NJ, Guardado-Estrada M and Perez-Plasencia C. Negative regulation of serine threonine kinase 11 (STK11) through miR-100 in head and neck cancer. Genes (Basel) 2020; 11: 1058.
[45] Mitra S, Mukherjee N, Das S, Das P, Panda CK and Chakrabarti J. Anomalous altered expressions of downstream gene-targets in TP53-miRNA pathways in head and neck cancer. Sci Rep 2014; 4: 6280.
[46] Worsham MJ, Lu M, Chen KM, Stephen JK, Havard S and Schweitzer VP. Malignant and nonmalignant gene signatures in squamous head and neck cancer. J Oncol 2012; 2012: 752860.
[47] Shulenina LV, Ushenkova LN, Ledin EV, Shagirova ZhM, Raeva NF, Zasukhina GD and Mikhaĭlov VF. Expression of P53, NPM1, Kras, c-Myc, p14(ARF) genes in blood cells of cancer patients before and after radiation therapy. Radiats Biol Radioecol 2012; 52: 572-581.
[48] Guihard S, Ramolu L, Macabre C, Wasylyk B, Noël G, Abecassis J and Jung AC. The NEDD8 conjugation pathway regulates p53 transcriptional activity and head and neck cancer cell sensitivity to ionizing radiation. Int J Oncol 2012; 41: 1531-1540.
[49] Colombo J, Fachel AA, De Freitas Calmon M, Cury PM, Fukuyama EE, Tajara EH, Cordeiro JA, Verjovski-Almeida S, Reis EM and Rahal P. Gene expression profiling reveals molecular marker candidates of laryngeal squamous cell carcinoma. Oncol Rep 2009; 21: 649-663.
[50] Zou Y, Zheng S, Deng X, Yang A, Xie X, Tang H and Xie X. The role of Circular RNA CDR1as/ciRS-7 in regulating tumor microenvironment: a pan-cancer analysis. Biomolecules 2019; 9: 429.
[51] Walk EE, Yohe SL, Beckman A, Schade A, Zutter MM, Pfeifer J and Berry AB; College of American Pathologists Personalized Health Care Committee. The cancer immunotherapy biomarker testing landscape. Arch Pathol Lab Med 2020; 144: 706-724.
[52] Zou Y, Hu X, Zheng S, Yang A, Li X, Tang H, Kong Y and Xie X. Discordance of immunotherapy response predictive biomarkers between primary lesions and paired metastases in tumours: a systematic review and meta-analysis. EBioMedicine 2021; 63: 103137.
[53] Bindea G, Mlecnik B, Tosolini M, Kirilovsky A, Waldner M, Obenauf AC, Angell H, Fredriksen T, Lafontaine L, Berger A, Bruneval P, Fridman WH, Becker C, Pages F, Speicher MR, Trajanoski Z and Galon J. Spatiotemporal dynamics of intratumoral immune cells reveal the immune landscape in human cancer. Immunity 2013; 39: 782-795.
[54] Fridman WH, Zitvogel L, Sautes-Fridman C and Kroemer G. The immune contexture in cancer prognosis and treatment. Nat Rev Clin Oncol 2017; 14: 717-734.
[55] Mehla K and Singh PK. Metabolic regulation of macrophage polarization in cancer. Trends Cancer 2019; 5: 822-834.
[56] Gibney GT, Weiner LM and Atkins MB. Predictive biomarkers for checkpoint inhibitor-based immunotherapy. Lancet Oncol 2016; 17: e542-e551.
[57] Camidge DR, Doebele RC and Kerr KM. Comparing and contrasting predictive biomarkers for immunotherapy and targeted therapy of NSCLC. Nat Rev Clin Oncol 2019; 16: 341-355.
[58] Chan TA, Yarchoan M, Jaffee E, Swanton C, Quezada SA, Stenzinger A and Peters S. Development of tumor mutation burden as an immunotherapy biomarker: utility for the oncology clinic. Ann Oncol 2019; 30: 44-56.

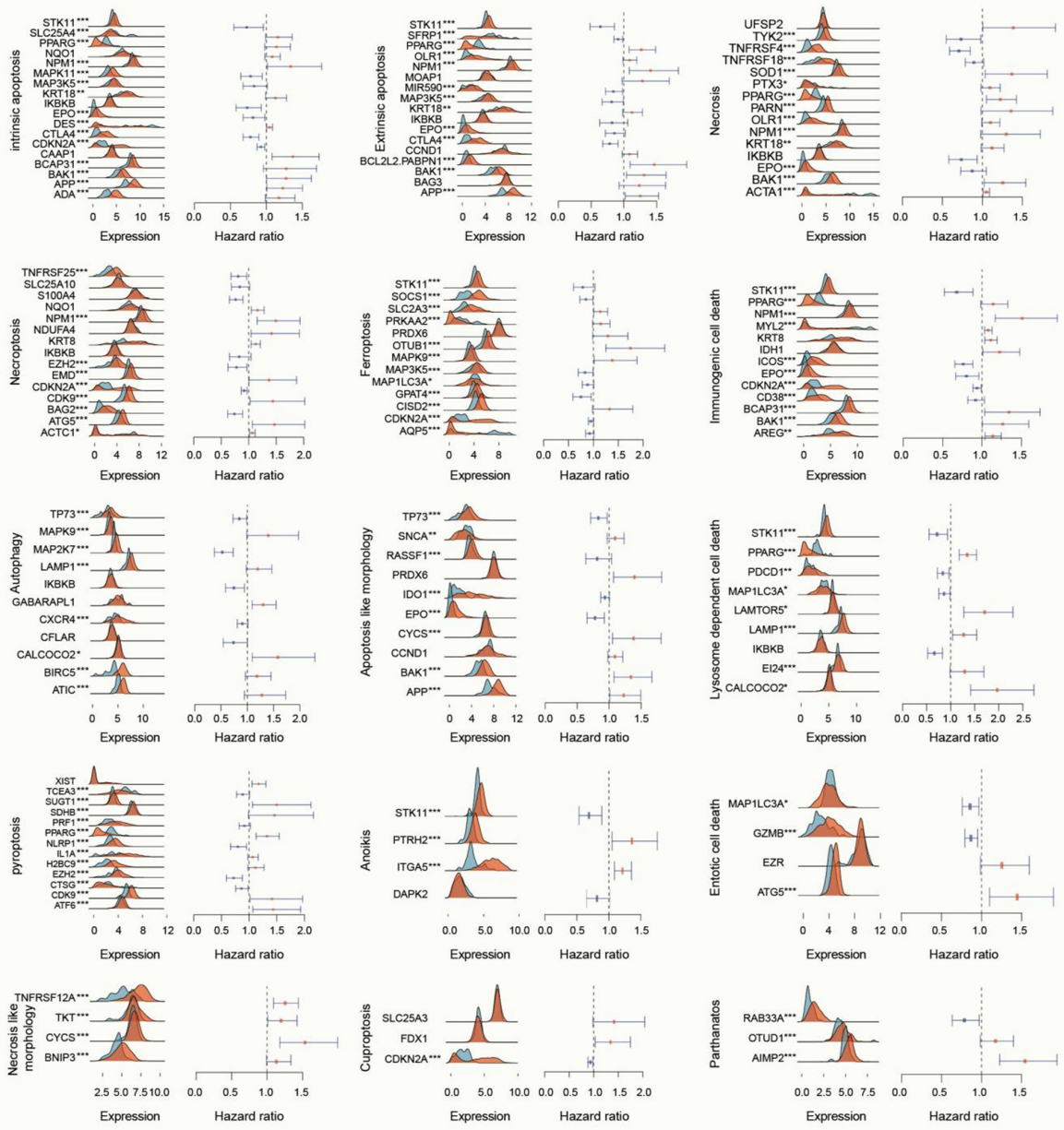

Figure S1. The 15 types of cell death related genes expression in normal and tumor tissue and associations of cell death related genes with HNSCC prognosis using multivariate cox regression.

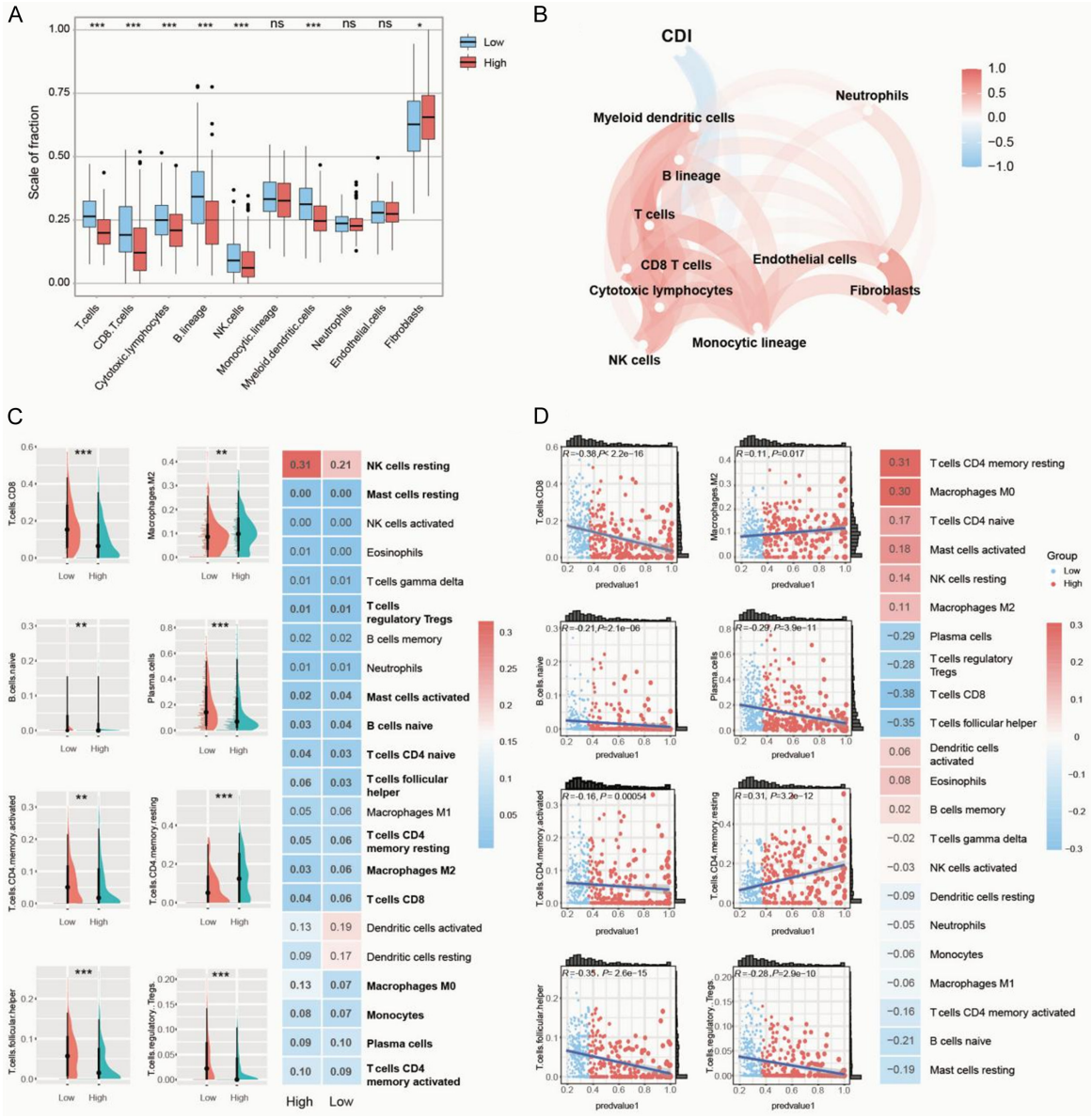

Figure S2. Correlation of CDI with immune cell infiltration. A. The Wilcoxon rank-sum test compared the absolute abundance scores of 8 immune cells and 2 stromal cells populations in high and low CDI group using MCP counter. B. The relationship of CDI with 8 immune cells and 2 stromal cells populations using MCP counter. C. The difference of 22 immune cells infiltration level between high and low CDI group using CIBERSORT algorithm. D. The relationship of CDI with 22 immune cells using CIBERSORT algorithm.

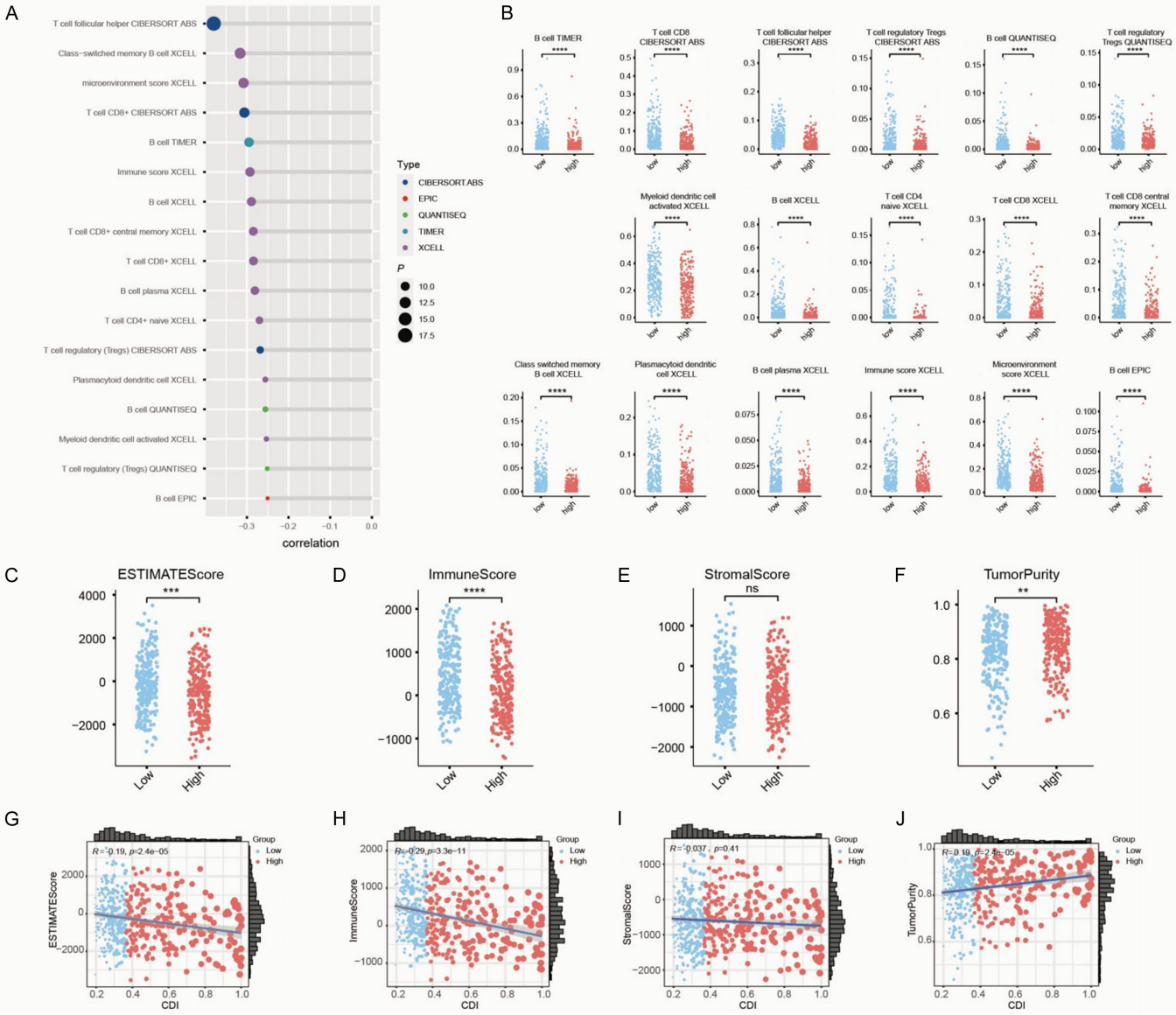

Figure S3. The investigation of immune landscape in high and low CDI group using several algorithm. A. The correlation of CDI with infiltration level of immune cells using CIBERSORT, EPIC, QUANTISEQ, TIMER and XCELL. B. The difference of immune cells infiltration level between high and low CDI group using CIBERSORT, EPIC, QUANTISEQ, TIMER and XCELL. C-F. The difference of ESITIMATE Score, IMMUNE Score, Stromal Score and Tumor Purity between high and low CDI group, respectively. G-J. The relationship of CDI with ESITIMATE Score, IMMUNE Score, Stromal Score and Tumor Purity, respectively.

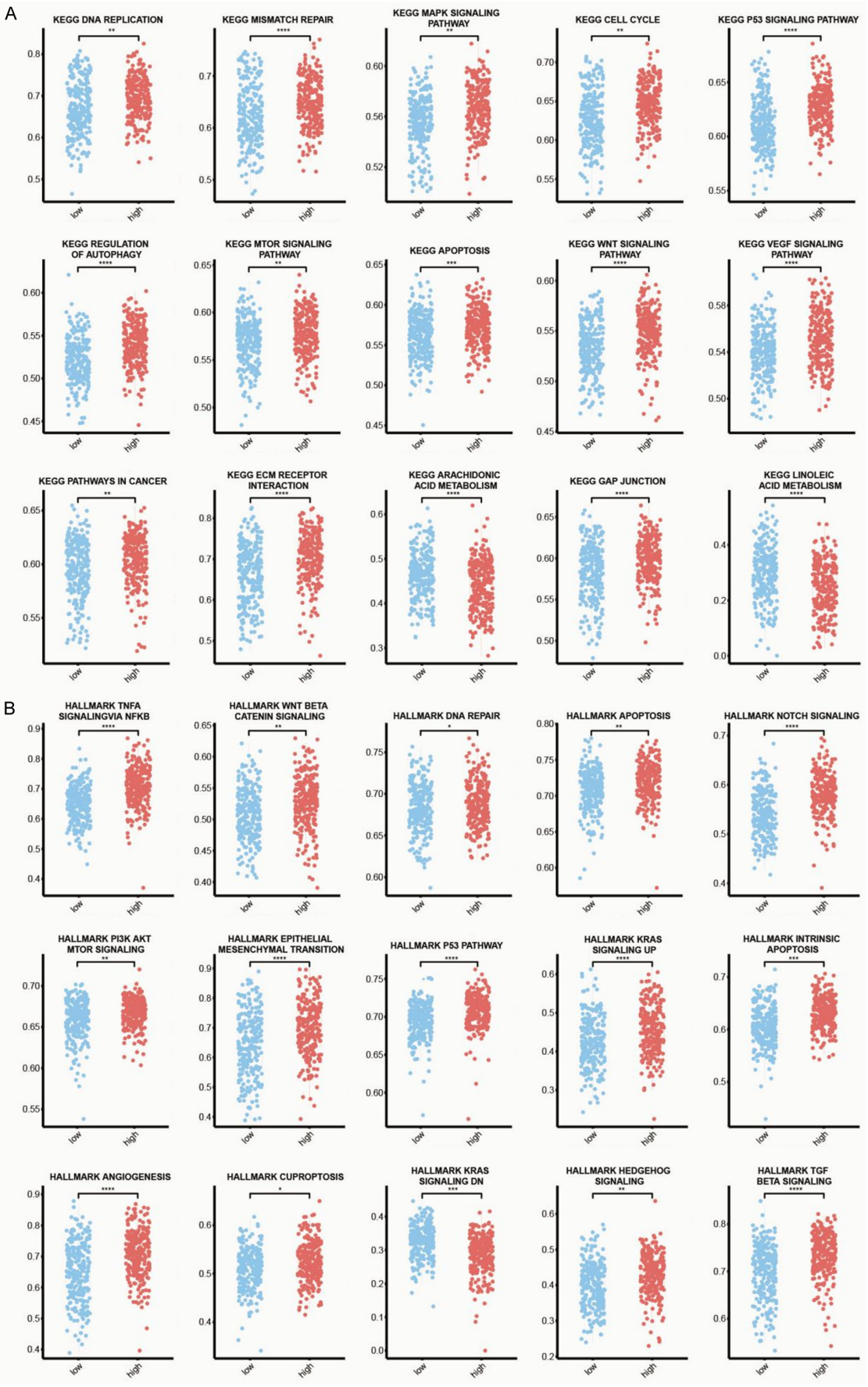
A
KEGG DNA REPLICATION
KEGG MISMATCH REPAIR
KEGG MAPK SIGNALING PATHWAY
KEGG CELL CYCLE
KEGG P53 SIGNALING PATHWAY
KEGG REGULATION OF AUTOPHAGY
KEGG MTOR SIGNALING PATHWAY
KEGG APOPTOSIS
KEGG WNT SIGNALING PATHWAY
KEGG VEGF SIGNALING PATHWAY
KEGG PATHWAYS IN CANCER
KEGG ECM RECEPTOR INTERACTION
KEGG ARACHIDONIC ACID METABOLISM
KEGG GAP JUNCTION
KEGG LINOLEIC ACID METABOLISM
B
HALLMARK TNFA SIGNALINGVIA NFKB
HALLMARK WNT BETA CATENIN SIGNALING
HALLMARK DNA REPAIR
HALLMARK APOPTOSIS
HALLMARK NOTCH SIGNALING
HALLMARK PI3K AKT MTOR SIGNALING
HALLMARK EPITHELIAL MESENCHYMAL TRANSITION
HALLMARK P53 PATHWAY
HALLMARK KRAS SIGNALING UP
HALLMARK INTRINSIC APOPTOSIS
HALLMARK ANGIOGENESIS
HALLMARK CUPROPTOSIS
HALLMARK KRAS SIGNALING DN
HALLMARK HEDGEHOG SIGNALING
HALLMARK TGF BETA SIGNALING
low
high

Figure S4. Gene set enrichment analysis and drug sensitivity of the CDI signature. A. The significantly enriched subset of KEGG canonical pathways based on GSEA. B. The significantly enriched HALLMARK gene sets based on GSEA.

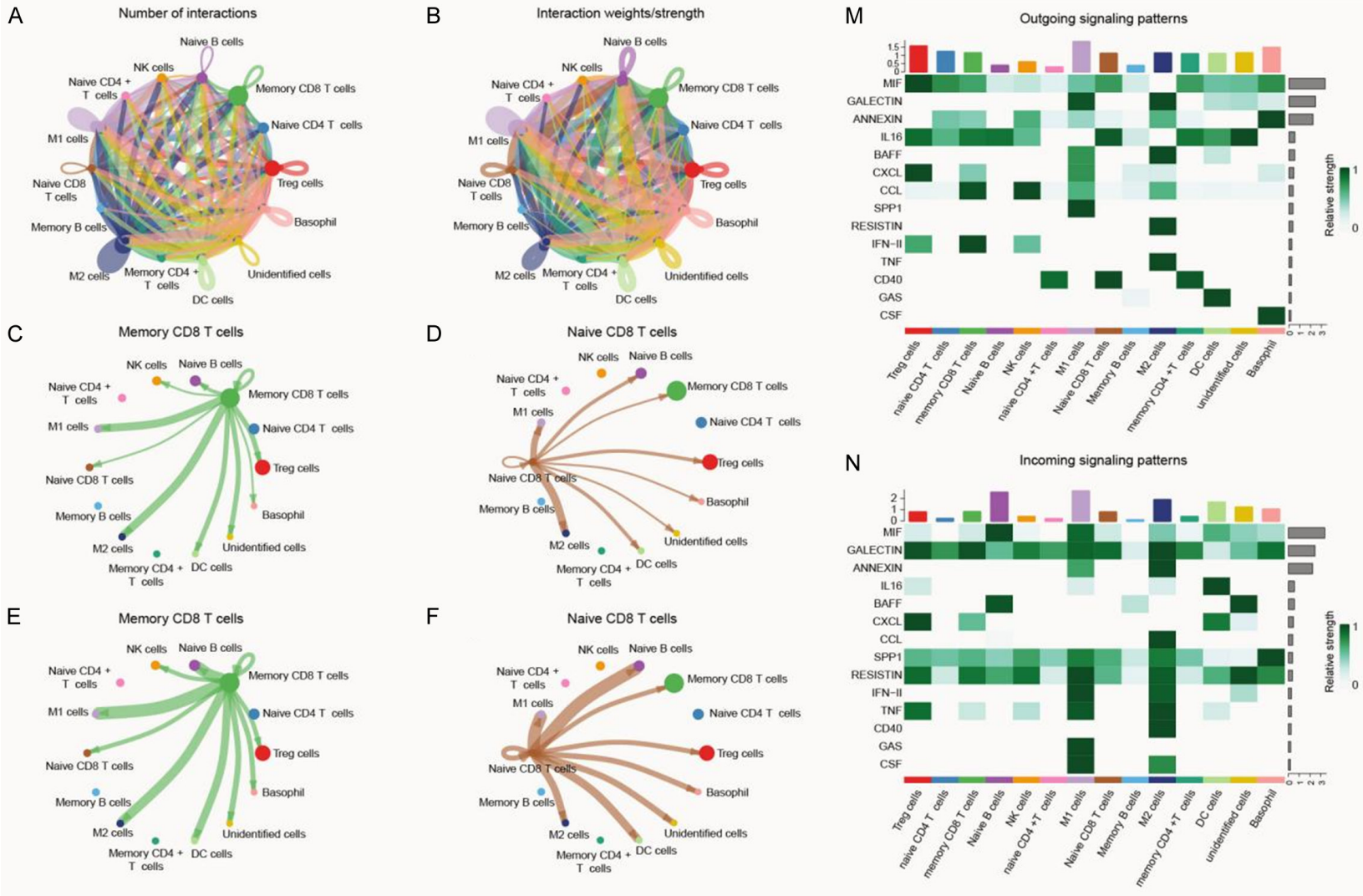

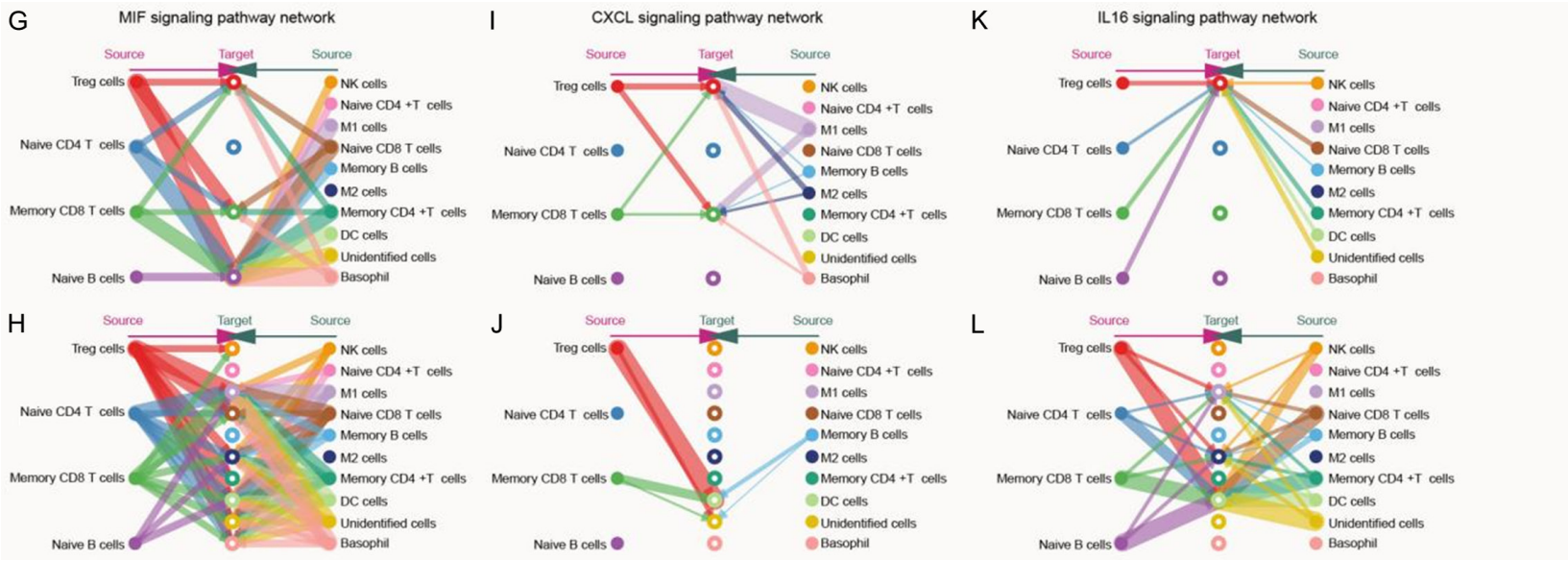

Figure S5. Cell communication network analysis in HNSCC. A. Chord plot showing the number of interactions among immune cell types. B. Chord plot showing the interaction weights/strength among immune cell types. C, D. The interaction number of memory or naïve CD8+ T cells with other immune cell types. E, F. The interaction weights/strength of memory or naïve CD8+ T cells with other immune cell types. G-L. Hierarchical chart showing inferred intercellular communication network of MIF, CXCL, IL16 signaling pathway with immune cell types using autocrine and paracrine signaling. Bar sizes are proportional to the number of cells in each cell group and line width represents the communication probability. M, N. The contribution weight of outgoing and incoming signaling patterns to immune cell types in cell communication network system.